

Rochester Institute of Technology

RIT Digital Institutional Repository

Theses

5-4-2021

Volume-based Estimates of Left Ventricular Blood Pool Volume and Ejection Fraction from Multi-plane 2D Ultrasound Images

Dawei Liu
dxl1169@rit.edu

Follow this and additional works at: <https://repository.rit.edu/theses>

Recommended Citation

Liu, Dawei, "Volume-based Estimates of Left Ventricular Blood Pool Volume and Ejection Fraction from Multi-plane 2D Ultrasound Images" (2021). Thesis. Rochester Institute of Technology. Accessed from

This Thesis is brought to you for free and open access by the RIT Libraries. For more information, please contact repository@rit.edu.

Volume-based Estimates of Left Ventricular Blood Pool Volume and
Ejection Fraction from Multi-plane 2D Ultrasound Images

by

Dawei Liu

A thesis submitted in partial fulfillment of the
requirements for the degree of Master of Science
in the Chester F. Carlson Center for Imaging Science
College of Science
Rochester Institute of Technology

May 4, 2021

Accepted by _____
Dr. Charles Bachmann Date
Coordinator, M.S. Degree Program

CHESTER F. CARLSON CENTER FOR IMAGING SCIENCE
COLLEGE OF SCIENCE
ROCHESTER INSTITUTE OF TECHNOLOGY
ROCHESTER, NEW YORK

CERTIFICATE OF APPROVAL

M.S. DEGREE THESIS

The M.S. Degree Thesis of Dawei Liu
has been examined and approved by the
thesis committee as satisfactory for the
thesis required for the
M.S. degree in Imaging Science

Dr. Cristian A. Linte, Thesis Advisor

Dr. Guoyu Lu

Dr. Yangming Li

Date

Dedication

Dedicated to my parents, for their endless love and inspiration.

Acknowledgments

I have the deepest gratitude for my thesis advisor Dr. Cristian A. Linte, who is always available to guide, advice, and support me throughout my graduate career. Dr. Linte is passionate for teaching and I was fortunate to work under his guidance to explore and learn. His compassion towards students gave us the confidence that he will always be there to fight for our success. I sincerely appreciate Dr. Karl Q. Schwarz, who educated us on the importance of accurately estimating the critical cardiac metrics that are vital to a patient's course of therapy. Dr. Schwarz provided us the resource to conduct this research such as the echocardiography datasets and practical knowledge in evaluating left ventricular ejection fraction. He generously spent much time with us at RIT and the echocardiography lab at University of Rochester to demonstrate the clinical procedure and provide research guidance. Without him, this research would not have been possible. A special thanks to Dr. Edward Hensel for supporting me during my undergraduate career at RIT and recommending me to continue on the study in Imaging Science. Dr. Hensel has a vision for students' continued success and always opens his door to assist. I would like to thank my colleague Shusil Dangi for his help on my research project and his friendship. I would also like to thank Isabelle Peck from Rensselaer Polytechnic Institute for her help on analyzing the echocardiography datasets and generating some valuable preliminary results for my continued research. Thank my labmates Golnaz Jalalahmadi, Kamrul Hasan, Roshan Reddy Upendra, Peter Jackson, and Richard Simon for their kindness to create an enjoyable lab environment.

Abstract

Accurate estimations of left ventricular (LV) blood pool volume and left ventricular ejection fraction (LVEF) are crucial for the clinical diagnosis of cardiac disease, patient management, or other therapeutic treatment decisions, especially given a patient’s LVEF often affects his or her candidacy for cardiovascular intervention. Ultrasound (US) imaging is the most common and least expensive imaging modalities used to non-invasively image the heart to estimate the LV blood pool volume and assess LVEF. Despite advances in 3D US imaging, 2D US images are routinely used by cardiologists to image the heart and their interpretation is inherently based on the 2D LV blood pool area information immediately available in the US images, rather than 3D LV blood pool volume information. This work proposes a method to reconstruct the 3D geometry of the LV blood pool from three tri-plane 2D US images to estimate the LV blood pool volume and subsequently the LVEF. This technique uses a statistical shape model (SSM) of the LV blood pool characterized by several anchor points – the mitral valve hinges, apex, and apex-to-mitral valve midpoints – identified from the three multi-plane 2D US images. Given a new patient image dataset, the diastolic and systolic LV blood pool volumes are estimated using the SSM either as a linear combination of the n-closest LV geometries according to the Mahalanobis distance or based on the n-most dominant principal components identified after projecting the new patient into the principal component space defined by the training dataset. The performance of the proposed method was assessed by comparing the estimated LV blood pool volume and LVEF to those measured using the EchoPac PC clinical software on a dataset consisting of 66 patients, and several combinations of 50-16 used for training and validation, respectively. The studies show the proposed method achieves LV volume and LVEF estimates within 5% of those computed using the clinical software. Lastly, this work proposes an approach that requires minimal user interaction to obtain accurate 3D estimates of LV blood pool volume and LVEF using multi-plane 2D US images and confirms its performance similar to the ground truth clinical measurements.

Contents

| | |
|--|------------|
| Abstract | iii |
| Contents | iv |
| List of Figures | vi |
| List of Tables | x |
| 1 Introduction | 1 |
| 1.1 Anatomy of the Cardiac System | 1 |
| 1.2 Anatomy of the Left Ventricle | 3 |
| 1.3 Left Ventricular Ejection Fraction | 4 |
| 1.4 Determining LVEF by Imaging | 5 |
| 1.4.1 Computed Tomography | 5 |
| 1.4.2 Magnetic Resonance Imaging | 6 |
| 1.4.3 Ultrasound Imaging | 6 |
| 1.5 Challenges in Volume-based LVEF Calculation | 7 |
| 1.6 Proposed solution | 10 |
| 2 Previous Work | 11 |
| 2.1 Simplified LV Blood Pool Volume Estimation Methods | 11 |
| 2.2 Geometric Models of LV | 14 |
| 2.3 3D Reconstruction of LV Geometry | 15 |

| | | |
|----------|--|-----------|
| 2.4 | Statistical Shape Models | 17 |
| 3 | Methodology | 19 |
| 3.1 | Data Preparation | 19 |
| 3.2 | Geometric Models Analysis | 21 |
| 3.3 | 3D Reconstruction | 23 |
| 3.4 | Statistical Shape Model | 25 |
| 3.4.1 | Mahalanobis Distance with Size Normalization | 27 |
| 3.4.2 | Vector Distance without Size Normalization | 28 |
| 4 | Results | 31 |
| 4.1 | Geometric Model | 31 |
| 4.2 | 3D LV Blood Pool Reconstruction | 33 |
| 4.3 | Statistical Shape Model | 35 |
| 5 | Discussion, Future Work, and Conclusion | 47 |
| 5.1 | Discussion | 47 |
| 5.2 | Future Work | 49 |
| 5.3 | Summary and Conclusion | 51 |
| | Bibliography | 53 |

List of Figures

| | | |
|-----|---|----|
| 1.1 | Blood circulation in the human body. | 2 |
| 1.2 | An illustration of the LV anatomy. (Illustration by David B. Nahabedian ©2019, provided under CC-BY-NC-ND) | 4 |
| 1.3 | The ultrasound probe (transducer) is placed over the patient skin. A monochromatic video feed of the US images captured by the transducer displays on the machine screen.[1] | 8 |
| 1.4 | A comparison of the functional differences of CT, MRI, and US imaging of the LV [2] | 8 |
| 1.5 | A histogram of LVEF based on the same dimensional data but calculated by area changes and volume changes correspondingly. | 10 |
| 2.1 | The modified Quinones method relies only on the LV end-diastolic diameter (LVEDD) and end-systolic diameter (LVESD) at mid-ventricle level. [3]. | 12 |
| 2.2 | An example 2D US transducer-produced image displayed on the US machine screen. Note the colored LV blood pool outlines need to be manually traced by the clinician after the session. The legend box on the top left corner of the image consists of relevant data based on the LV blood pool tracing calculated by the US machine. | 13 |
| 2.3 | A prolate spheroid split off-center (e.g $Z=-2$) along Z -axis results in a truncated prolate spheroid (TPS). [4]. | 14 |

| | | |
|-----|--|----|
| 2.4 | An overview of various geometric models evaluated in the work by Weijer <i>et al.</i> [5]. The full volume dataset (FV) is the "gold standard" reference dataset that was assembled from LV short-axis slices of the full LV blood pool. Both the hemisphere cylinder (HC) and biplane ellipsoid (BP) correlated better to the reference FV dataset than single-plane ellipsoid (SP) and modified Teichholz (TF) models. Modified Simpson (SR) model, as the only clinically recommended method for LV volume estimation, correlates the best with the reference FV dataset. | 15 |
| 2.5 | LV volume 3D reconstruction from short axis images. | 16 |
| 2.6 | LV volume 3D reconstruction from long axis images. | 17 |
| 3.1 | The zoomed-in section of the Figure 2.2 in which the LV blood pools at end-diastole and end-systole were traced by the clinical expert in blue and green, respectively. | 20 |
| 3.2 | Manually segmented LV blood pools in end-diastole (ED) and end-systole (ES) from the patient-specific US images. | 20 |
| 3.3 | The zoomed-in section of the Figure 2.2 in which information related to the LV blood pools at end-diastole and end-systole were generated by the clinical US machine and displayed in the legend box at top left corner of the image. | 21 |
| 3.4 | Mathematical approximations of the LV geometry using a truncated prolate spheroid (TPS) model and a paraboloid model. | 22 |
| 3.5 | An illustration of systolic and diastolic LV volume estimation by the GE EchoPac clinical software using the Method of Discs by assuming that LV geometry is asymmetrical. | 23 |
| 3.6 | 3D reconstruction workflow: extract LV blood pools in three views; align apices and mitral valve bases; reconstruction by convex hull interpolation between three views. | 24 |
| 3.7 | 3D Reconstruction of LV volume using convex hull model. | 24 |

| | | |
|------|--|----|
| 3.8 | Anchor point locations on an example diastolic LV endocardial border (the outer-most blue trace in the images with black background in the left column). | 26 |
| 4.1 | The difference of LVEFs calculated based on volume and area using TPS and paraboloid models. | 32 |
| 4.2 | A box and whisker plot of the LVEF calculated from MOD and 3D reconstructed volumes. | 34 |
| 4.3 | Plotting the LVEF results based on 3D reconstructed volumes to the reference MOD values provides a slope of 0.97 and a coefficient of determination of 0.93. | 35 |
| 4.4 | The point cloud constructed from land marks of the 50 training image datasets. | 36 |
| 4.5 | Bland-Altman plot of the SSM-derived LVEFs and the reference MOD LVEFs. . | 37 |
| 4.6 | Patient-specific percent error of the estimated LVEF based on the reference MOD data using Mahalanobis distance and PC vector distance methods. | 39 |
| 4.7 | Patient-specific percent error of the estimated LVEF based on the reference MOD data using Mahalanobis distance and PC vector distance methods. | 40 |
| 4.8 | Patient-specific percent error of the estimated LVEF based on the reference MOD data using Mahalanobis distance and PC vector distance methods. | 41 |
| 4.9 | Patient-specific percent error of the estimated LVEF based on the 3D reconstruction data using Mahalanobis distance and PC vector distance methods. . . | 42 |
| 4.10 | Patient-specific percent error of the estimated LVEF based on the 3D reconstruction data using Mahalanobis distance and PC vector distance methods. . . | 43 |
| 4.11 | Patient-specific percent error of the estimated LVEF based on the 3D reconstruction data using Mahalanobis distance and PC vector distance methods. . . | 44 |

| | | |
|------|---|----|
| 4.12 | Plotting the LVEF results based on estimated systolic and diastolic volumes using Mahalanobis and PC Vector distances against the reference MOD values provides a linear fit of 0.887 for LVEF based on Mahalanobis distance and 1.065 for LVEF based on PC vector distance. The linear fit on the LVEF using PC vector distance is slightly better than that on the LVEF using Mahalanobis distance according to the coefficient of determination of 0.987 for the former versus 0.986 for the latter. | 45 |
| 4.13 | The percent difference between the LVEF computed based on SSM-estimated volumes and the LVEF computed based on the 3D reconstructed volumes using different numbers of PCs. The legend details the color codes of the data series for each of the 16 testing patient IDs. | 46 |
| 5.1 | An example US image annotated with image quality metrics: L, D, m, h | 49 |

List of Tables

| | | |
|-----|---|----|
| 1.1 | Categorization of LVEF based on its value and subject gender. | 5 |
| 4.1 | Summary statistics of the LVEF-related quantities based on the TPS model, paraboloid model, and the clinical data analyzed using GE's EchoPac PC clinical software. | 32 |
| 4.2 | Statistics of the LVEF-related quantities based on the reference MOD and 3D blood pool reconstructions from the multi-plane 2D US imaging data. | 33 |
| 4.3 | Summary statistics of the LVEF-related estimates using the Mahalanobis distance and PC space vector distance based on the reference MOD values for the 16 testing patients. | 37 |
| 4.4 | Summary statistics of the LVEF-related estimates from the Mahalanobis distance and PC space vector distance based on the 3D reconstructed values for the 16 testing patients. | 38 |
| 4.5 | Summary statistics of the LVEF-related quantities using reduced number of PCs to estimate for the 16 testing patients. | 38 |

Chapter 1

Introduction

This master's thesis focuses on analyzing and improving the calculation of the left ventricular ejection fraction (LVEF) from multi-plane two-dimensional ultrasound images. The project encompasses four components of work that naturally progresses as one component depends on the earlier one. Our clinical collaborator, Dr. Karl Q. Schwarz [6], originally raised the concern about the current practices on LVEF calculations in clinical settings. Schwarz pointed out the current clinical practices lead to LVEF inaccuracies and consequently lead to unnecessary or sometimes inappropriate therapeutic treatments. In this thesis project, we implemented a combination of existing techniques and novel methodologies to improve the LVEF calculation.

1.1 Anatomy of the Cardiac System

The left ventricle is one of the four chambers in the heart, which consists of two ventricles and two atria. A cardiac cycle, which is commonly known as a "heart beat", consists of blood being pumped into the systemic circulation and the pulmonary circulation. After circulating through the body, de-oxygenated blood returns to the right atrium through the systemic circulation and then into the right ventricle. From the right ventricle, the de-oxygenated blood is fed into the lungs through pulmonary circulation where the blood becomes oxygenated again. Once the blood finishes circulating through the lungs, it goes back into the left atrium and then into the left ventricle to eventually be pumped once again into the systemic circulation and

1.1. Anatomy of the Cardiac System

supplied to the rest of the body.[7]

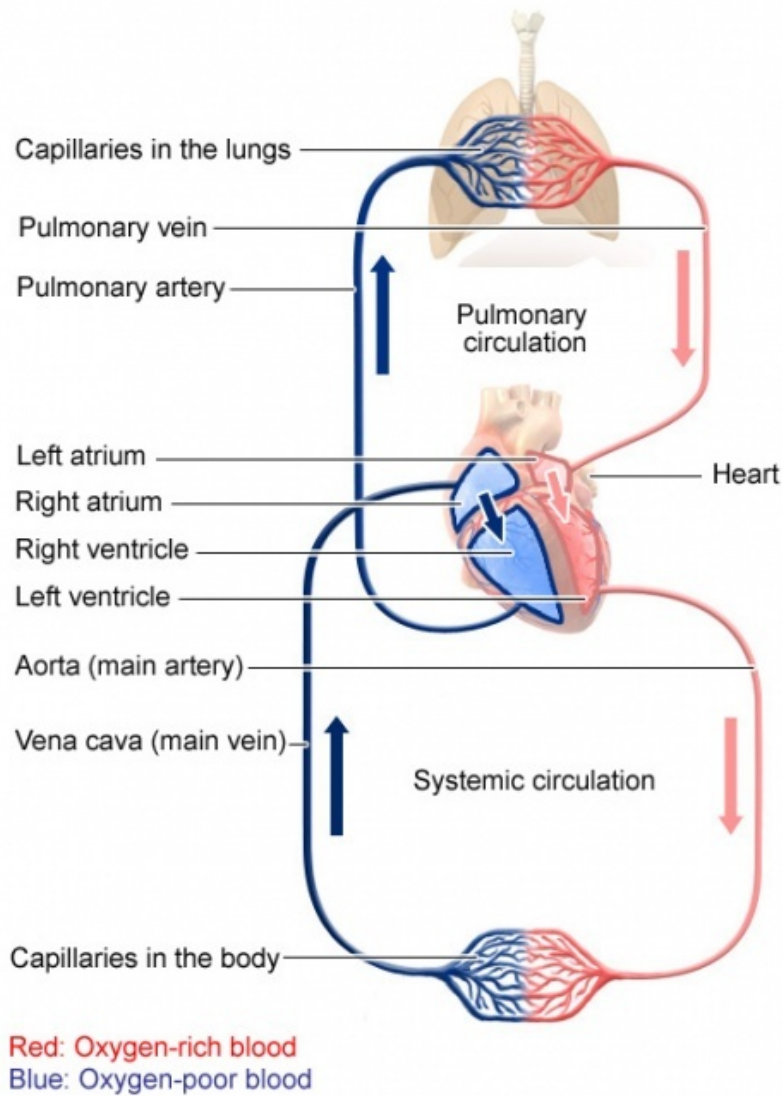


Figure 1.1: Blood circulation in the human body.

Evidently, the cardiac function is critical to the sustainability of the livelihood and promotion of the health of a human body. The pumping motion of the heart is achieved when the cardiac muscle, also known as "myocardium", contracts and relaxes during a cardiac cycle. The contractions and relaxations are referred to as the systolic and diastolic phases in a cardiac cycle, respectively. Electrical impulses trigger the contractions of the atria and ventricle

and the frequency of the impulses determines the number of heart beats per minute, which is a common measure of the cardiac function. Since the left ventricle is the chamber that pumps the oxygenated blood through the body, the amount of oxygenated blood that can be pumped during a cardiac cycle is of particular interest to the analysis of the cardiac health.

1.2 Anatomy of the Left Ventricle

The left ventricle (LV) consists of anatomical features that enable it to function as a power pump to help circulate oxygenated blood throughout the body. Notably, an LV has an apex, base, aortic valve, mitral valve, and free wall [8]. There are two distinct phases in a cardiac cycle: ventricular systole and diastole (aortic systole and diastole is out of the scope of this discussion) [9]. At the beginning of the systole, the aortic and mitral valve are both closed. During systole, the LV pressure increases due to free wall contraction until the aortic valve is forced open under pressure. Oxygenated blood exits the LV through aortic valve until it closes again to begin diastole. During diastole, the mitral valve opens and oxygenated blood from the respiratory system enters the LV as the apex and free wall relax. This process is referred to as a stroke and its volume is the difference between the volumes of the LV blood pool when fully relaxed (end-diastole) and fully contracted (end-systole) in a cardiac cycle. The stroke volume obviously depends on the size of the heart and consequently depends on the person in terms of age, weight, gender, and other factors. In order for clinicians to assess cardiac health of different patients, a measure that is more independent of patient physiological differences is necessary. The ratio between the LV stroke volume and volume at end-diastole (diastolic volume) measures the cardiac function more effectively across the population. This ratio is defined as the left ventricular ejection fraction (LVEF) [10] and will be discussed in the further detail.

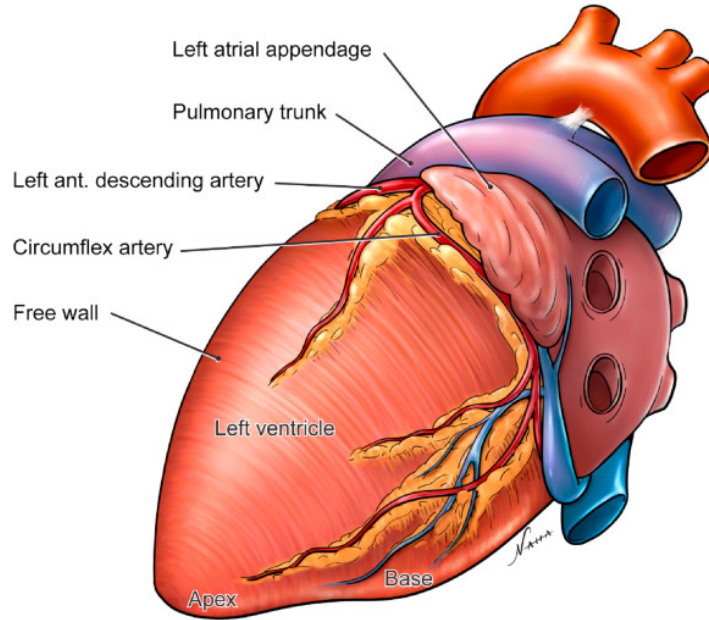


Figure 1.2: An illustration of the LV anatomy. (Illustration by David B. Nahabedian ©2019, provided under CC-BY-NC-ND)

1.3 Left Ventricular Ejection Fraction

As an essential indicator of the cardiac function and health, left ventricular ejection fraction (LVEF) measures the amount of oxygenated blood the LV can pump out during the LV ejection in one cardiac cycle. LVEF can be mathematically defined by the ratio between the chamber stroke volume and the end-diastolic volume. The chamber stroke volume is the difference between the left ventricular volumes at end-diastole $V_{diastole}$ and end-systole $V_{systole}$.

$$LVEF = \frac{V_{diastole} - V_{systole}}{V_{diastole}} = \frac{Stroke\ Volume}{V_{diastole}} \quad (1.3.1)$$

The LVEF of a particular person depends on factors such as gender, age, and cardiovascular disease presence, so there is no particular LVEF to determine a person's cardiovascular health. However, per American Society of Echocardiography [11] and European Association

Table 1.1: Categorization of LVEF based on its value and subject gender.

| Gender | Normal | Mildly abnormal | Moderately abnormal | Severely abnormal |
|--------|------------|-----------------|---------------------|-------------------|
| Male | 52% to 72% | 41% to 51% | 30% to 40% | <30% |
| Female | 54% to 74% | 41% to 53% | 30% to 40% | <30% |

of Cardiovascular Imaging [12], a person’s heart health can be categorized by different ranges of LVEF values as enumerated in Table 1.1. It is important to note that these categorization ranges were determined for LVEFs calculated from two-dimensional ultrasound images. These ranges could be different if LVEFs were calculated from images acquired by other modalities.

1.4 Determining LVEF by Imaging

LVEF is defined by LV volumes at different stages in a cardiac cycle, so it can be calculated if LV volumes are measured by some means. Medical imaging allows clinicians to capture a patient’s organ volumes either invasively or non-invasively. Since calculating a patient’s LVEF is ubiquitous during a clinical visit, non-invasive imaging of the LV is most preferred. Commonly accessible non-invasive imaging modalities include magnetic resonance imaging (MRI), computed tomography (CT), and ultrasound imaging (US). It is vital to understand the advantages and disadvantages of each imaging modality before we choose which modality to focus the research on.

1.4.1 Computed Tomography

Computed tomography (CT) is one of the more established imaging modality as it is based on X-ray technology. A CT machine has an X-ray source that rotates around a patient while the patient traverse through the CT machine to image "slices" of the body internals [13]. CT acquires images based on the x-ray attenuated by an object. In the case of medical imaging, x-ray energy source creates ionizing radiation when transmitted through a human body. CT imaging, or X-ray in general, is best suited for structural imaging because solid objects attenuate x-ray energy better than soft tissue. In order to combat this shortcoming

in cardiac applications, radiologists typically inject contrast agent into the patient's blood stream to help highlight the blood flow in the LV which increases image contrast. Obviously, injecting contrast agent and sustaining ionizing radiation is not ideal to perform routinely on any patient. For acquiring common clinical measurements such as LVEF, CT is not suitable.

1.4.2 Magnetic Resonance Imaging

In contrast to CT imaging, magnetic resonance imaging (MRI) is best suited for imaging applications that involve soft tissue. MRI employs strong magnets to forcibly align protons in a patient's body with the electromagnetic field of the machine [14]. By pulsating radio waves in a controlled manner, the MRI machine can detect how quickly protons mis-align and re-align with the magnetic field. In addition to varying paces protons take to change their alignment, they also emit different amount of energy while doing so. These two attributes help MRI machines detect different types of tissues and then form images. MRI does not emit ionizing radiation, but may require contrast agent injection in certain applications. During an image capture session, the patient must hold his or her breathe for a specified time, or the images will be blurred. Another downfall of MRI is that patients having metallic implants cannot go inside the magnet. For patients with cardiovascular disease, this limitation is particularly prohibitive because they may have pacemakers and implantable cardioverter- defibrillators.

1.4.3 Ultrasound Imaging

With specifically constructed acoustic waves applied to an object, US uses the reflected acoustic waves to discern the geometry of the object. Even though both MRI and US utilize non-ionizing radiation, the disadvantage of MRI is that the acquisition process is more intricate and expensive. Due to the ease of set up, low-cost, and fast data acquisition, US is the ubiquitous imaging modality for cardiac diagnosis. Nonetheless, the basic working theories will be presented.

US imaging is commonly known as diagnostic medical ultrasound as it is used to acquire relevant patient health information to assist medical professionals in performing diagnosis. US

1.5. Challenges in Volume-based LVEF Calculation

waves are produced by transducers at frequencies above the threshold of human hearing [1] and then retrieved to generate images of the path the waves traveled. The generated images are monochrome and the brightness of the object appearance relates to its density. In the US images, the denser the material the waves trespass, the lighter the material will appear in the image. During an acquisition session, a medical professional places the transducer on the patient's skin around the region of interest. Usually, a layer of gel will be applied to prevent air pockets from forming between the transducer and the skin. For 2D US transducers, the generated images illustrate an area the US waves traveled through that is perpendicular to the contact surface between the skin and the transducer. For 3D US transducers, the generated images or rather volumes represent a conical or pyramidal space that the US waves traveled through that is also perpendicular to the contact surface.

Despite commercial and academic efforts over the years, US images have relatively low quality and high noise comparing to other medical imaging modalities such as MRI or CT. However, US imaging possesses qualities that are suitable for daily clinical sessions because it is non-invasive, emits no ionizing radiation, and can be captured on small-footprint and low-cost equipment. US imaging is able to provide diagnostic information needed for routine medical needs, so it is ubiquitous in all cardiology suites. Hence, this project will utilize US images acquired by our collaborator to perform research tasks described further.

1.5 Challenges in Volume-based LVEF Calculation

Despite its simplicity in calculation, LVEF is an essential indicator of cardiac function and serves as a critical biomarker for cardiac diseases. Thus, LVEF is considered one of the most vital measures in the field of cardiology. Other than being an indicator of cardiac health in clinical examinations of patients, LVEF is also a criterion used to determine patient eligibility for various therapeutic management strategies in many hospital systems or participation in various research and clinical trials.

In practice, however, cardiologists most often use 2D US imaging to visually estimate ejection fraction based on changes in the LV blood pool areas between end-diastole and end-

1.5. Challenges in Volume-based LVEF Calculation

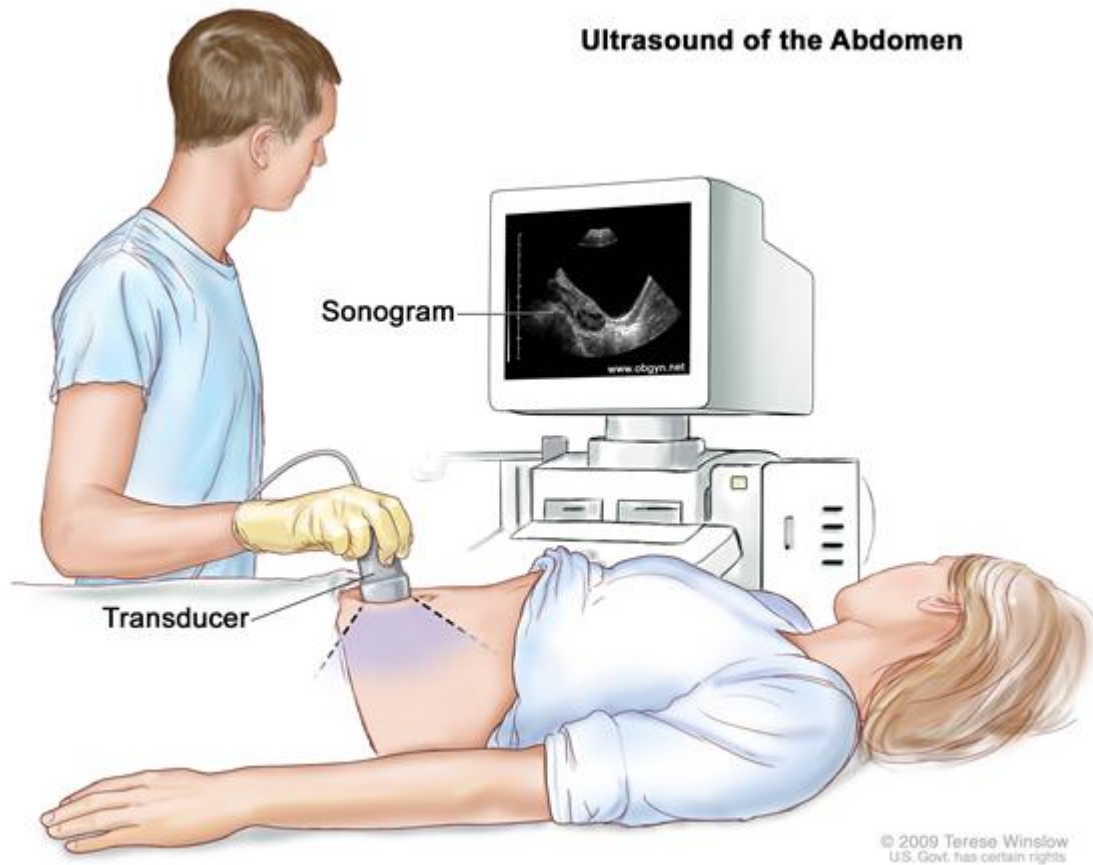


Figure 1.3: The ultrasound probe (transducer) is placed over the patient skin. A monochromatic video feed of the US images captured by the transducer displays on the machine screen.[1]

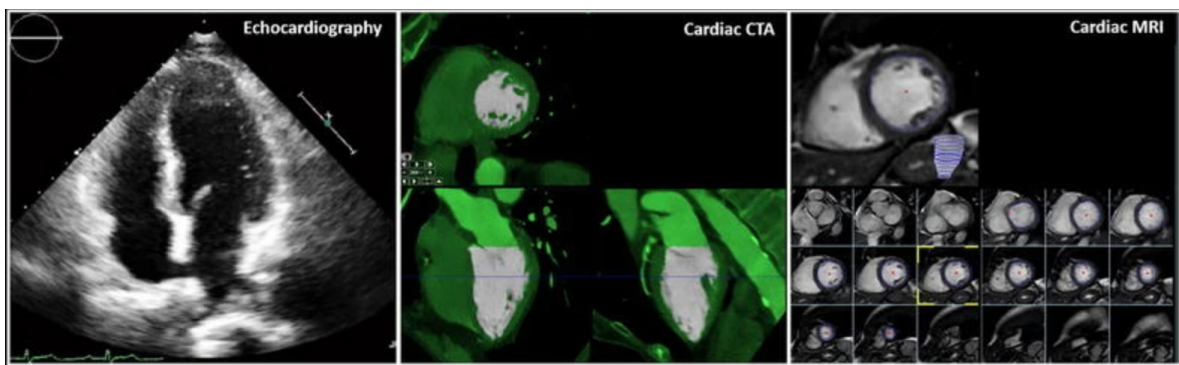


Figure 1.4: A comparison of the functional differences of CT, MRI, and US imaging of the LV [2]

1.5. Challenges in Volume-based LVEF Calculation

systole rather than change in volumes. Square-Cube Law explains that the ratio of two volumes will always be greater than the ratio of their surfaces. Consequently, the law infers that an object's change in volume in three-dimensional space is always greater than the change of area in two-dimensional space. Therefore, visual assessment of LVEF based on area changes is suspected to produce lower LVEFs than the true volumetric assessments.

Our clinical collaborator's preliminary analysis using a database of 68 patients suggested that the LVEF estimates based on area changes are approximately 16.7% lower than the LVEF estimates based on volume changes. Furthermore, the comparison exposed that there is a bias for the visually estimated LVEF towards the lower values in general. Understandably, the echo-cardiologists tend to aim for safety and, if in doubt, would rather underestimate than overestimate the LVEF, so that patients may be eligible for additional follow-up or potentially implantable assistive devices or other therapies to prevent cardiac malfunction.

Another statistical characteristic of the visually estimated LVEFs is "binning". The reported LVEFs based on visual estimations appeared discrete and were typically reported in increments of 5%. Since visual estimation is a rough method to determine LVEF, it is difficult for echo-cardiologists to estimate LVEF in finer increments. Such characteristic is detrimental though. For a healthy person, the LVEF should exceed 55%, while a LVEF below 35% is considered reduced contraction efficiency[15]. Such thresholds are not universal as they vary on a case by case basis. Therefore, when the visual estimations of LVEF are only reported in increments of 5%, estimated LVEF values around the 55% or 35% thresholds will lead to incorrect diagnosis. Due to the lack of precision, the LVEF could fall on either side of these thresholds, hence rendering a patient's heart function either normal or abnormal, simply due to the inherent variability of the visually estimated LVEFs. Consequently, people without cardiac disease may be diagnosed with reduced LVEF and vice versa.

Diagnosis of cardiac disease then leads to therapeutic decisions, some of which, such as implantable cardiac defibrillators (ICD), are associated with an initial operation cost between \$30,000 to \$50,000, and a follow-up treatment on the order of \$5,000 to \$17,000 [16]. In addition to the significant healthcare cost, the quality of life for a patient changes inevitably.

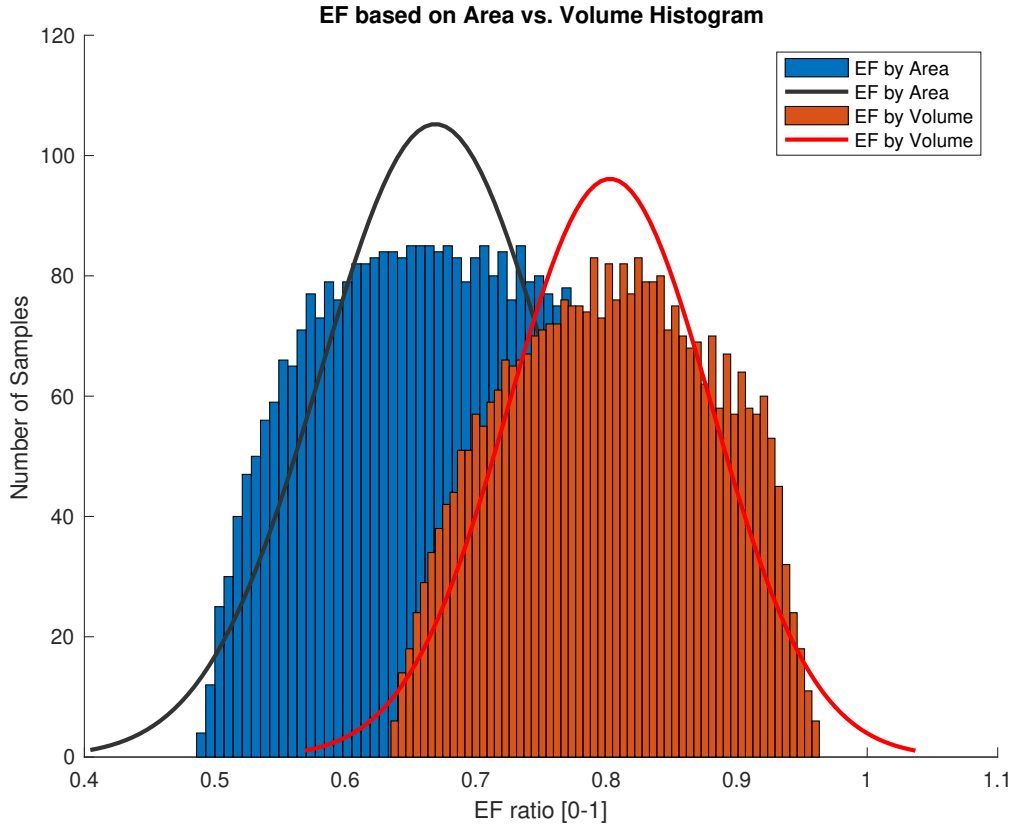


Figure 1.5: A histogram of LVEF based on the same dimensional data but calculated by area changes and volume changes correspondingly.

1.6 Proposed solution

The premise of this work is four-fold: 1) demonstrate, using both mathematical models of the LV geometry, as well as patient-specific data, that 2D area-based LVEF measurements significantly underestimate 3D volume-based measurements, 2) propose a method to reconstruct the 3D LV blood pool in systole and diastole from 2D multi-plane images and assess it against a current method used in the clinic [17], 3) calculate LVEF based on 3D reconstructed LV blood pool volumes, 4) estimate LVEF more efficiently without the need to reconstruct 3D LV blood pool volumes.

Chapter 2

Previous Work

In order to non-invasively assess LVEF from medical images, LV blood pool volumes need to be determined accurately. Existing work done by various researchers include simplified LV blood pool volume estimation methods, simulating LV shape using geometric models, realistically representing LV geometries by 3D reconstruction, and efficiently generalizing the LV geometric characteristics using statistical shape models(SSM).

2.1 Simplified LV Blood Pool Volume Estimation Methods

Due to the lack of "gold standard" for estimating LV blood pool via non-invasive imaging techniques, several attempts have been made to establish LV volume estimation methods based on some assumptions [18]. Most proposed methods rely on one-dimensional or two-dimensional data such as M-mode Echocardiography or 2D echocardiography [19].

The modified Quinones method is often employed due to its time efficiency and the need for only two linear measurements [20]. By omitting the contribution of LV longitudinal contraction to the overall LVEF, only end-diastolic and end-systolic measurements of the LV short-axis diameter at mid-ventricle level are incorporated into the LVEF estimation. The LV short-axis is perpendicular to the LV long axis (i.e., LV apex to base). Similar to the modified Quinones method, the Teichholz method leverages on the LV end-diastolic and end-systolic inner diameters to estimate the LV volumes [21]. LVEF can be subsequently calculated from the estimated

2.1. Simplified LV Blood Pool Volume Estimation Methods

LV volumes. Both the modified Quinones and Teichholz methods make major assumptions on the geometry of the LV and longitudinal LV contraction does not contribute significantly to the LVEF. The limitations of these two methods arise from situations where patients have asymmetric LV contraction or when US transducers cannot be oriented perpendicularly to the LV longitudinal axis.

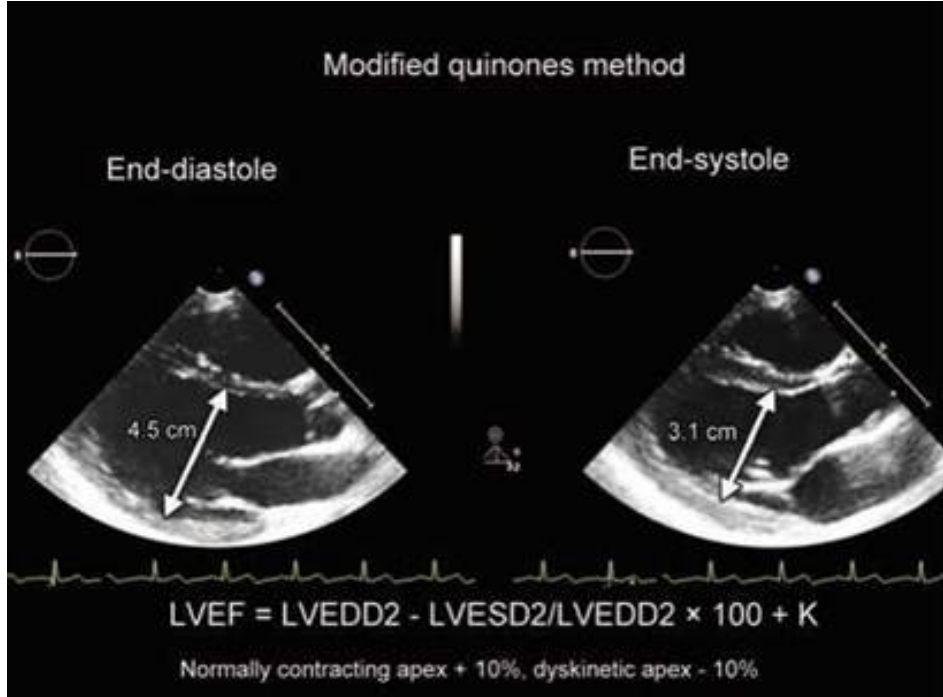


Figure 2.1: The modified Quinones method relies only on the LV end-diastolic diameter (LVEDD) and end-systolic diameter (LVESD) at mid-ventricle level. [3].

In Equation 2.1.1, D is the LV inner diameter at the mid-ventricle level.

$$Volume_{Teichholz} = \frac{7}{2.4 + D} * D^3 \quad (2.1.1)$$

Another simplified LV blood pool volume estimation method is Simpson's method, which is the only recommended clinical technique for 2D US imaging currently [22]. Simpson's method, also known as the Method of Discs, requires the LV to be imaged in the long-axis view and the endocardial border be traced out by a clinician. Twenty equal-height discs, oriented perpendicularly to the LV long axis, which connects the apex to the center of the

2.1. Simplified LV Blood Pool Volume Estimation Methods

mitral valve, divide the LV blood pool within the manually traced endocardial border. By assuming the LV is axi-symmetric, the volumes of the twenty cylindrical discs are summed to provide a LV estimation. Generally, the estimated LV volumes using Simpson's method from apical 2-chamber and apical 4 chamber views will be aggregated to that from long-axis view to generate an average estimated LV volume.

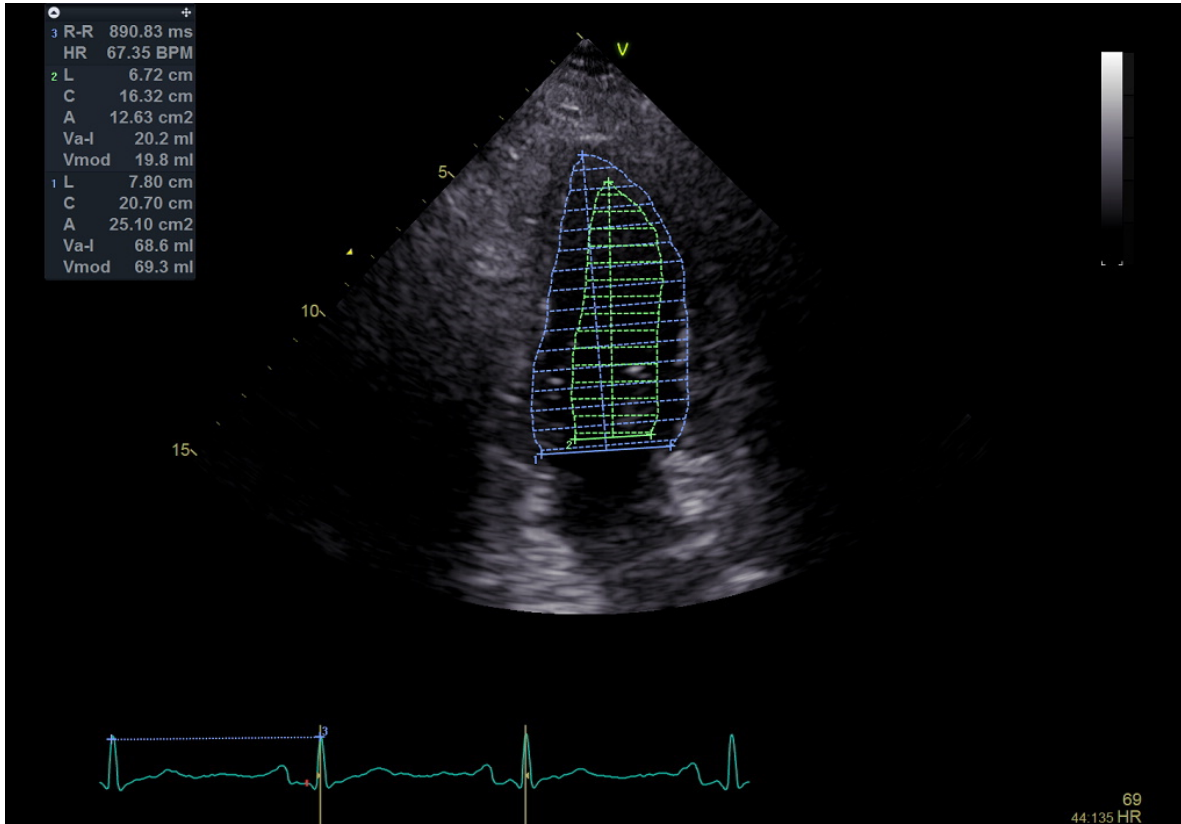


Figure 2.2: An example 2D US transducer-produced image displayed on the US machine screen. Note the colored LV blood pool outlines need to be manually traced by the clinician after the session. The legend box on the top left corner of the image consists of relevant data based on the LV blood pool tracing calculated by the US machine.

All aforementioned methods suffer from improper US transducer orientation that cause anatomical feature location misalignment between different views, geometric assumptions of the LV being axi-symmetric, inaccuracies in gating the image captures at the same time point in cardiac cycles, and omission of the the presence of the cardiac disease that lead to LV physiological variations, which raise the main reason for quantifying LVEF [23].

2.2 Geometric Models of LV

As with many anatomical features, the geometry of the heart and its chambers varies from person by person to some degree. Compounded with malignant complications introduced by unfortunate illnesses, it is a challenge to generalize anatomical features such as the left ventricle. Even in the face of challenges, many researchers attempted to theorize models to describe the LV geometry. On one end where a generic approach was taken, mathematical models such as cylindrical [24], truncated prolate spheroid [25], and paraboloid [26] were proposed. These mathematical models enable users to generate theoretical data based on known dimensions of the LV geometries and without requiring actual LV 3D geometric information. In a comprehensive comparison of various geometric models of the rodent LV by Weijer *et al.* [5], they found that the hemisphere cylinder (HC) model correlate just as well as the modified Simpson’s method (SR) to the reference full volume LV model (FV). As depicted in Figure 2.4, the HC model is equivalent to the paraboloid model described in other literature. Thus, both the truncated prolate spheroid and the paraboloid models will be used in this project to prove the significant difference between area-based and volume-based LVEF calculations as the first step.

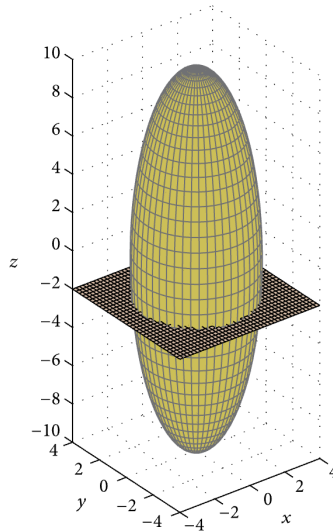
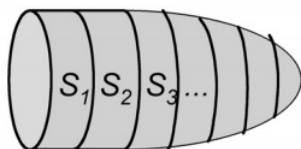


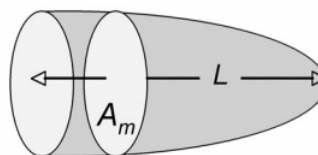
Figure 2.3: A prolate spheroid split off-center (e.g $Z=-2$) along Z-axis results in a truncated prolate spheroid (TPS). [4].

Full volume data set (FV)

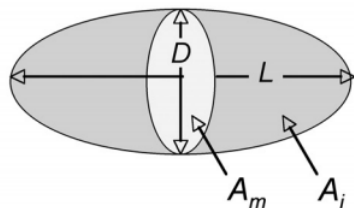
$$LVV = S_1 + S_2 + S_3 + \dots$$


Hemisphere cylinder model (HC)

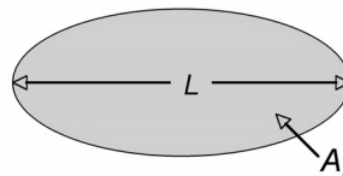
$$LVV = A_m \times L/2 + 2/3 \times A_m \times L/2 = 5/6 \times A_m \times L$$


Biplane Ellipsoid model (BP)

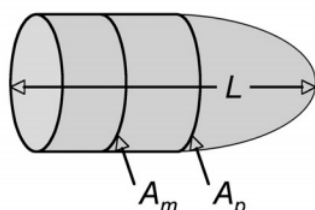
$$LVV = \pi/6 \times L \times (4/\pi \times A_m/D) \times (4/\pi \times A_i/L)$$


Single-plane Ellipsoid model (SP)

$$LVV = (8 \times A_i \times A_i) / (3\pi \times L) = 0.85 \times (A_i \times A_i) / L$$


Modified Simpson rule model (SR)

$$LVV = A_m \times L/3 + (A_m + A_p)/2 \times L/3 + 1/3 \times A_p \times L/3$$


Modified Teichholz Formula (TF)

$$LVV = [7 / (2.4 + D)] \times D \times D \times D$$

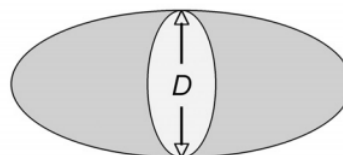


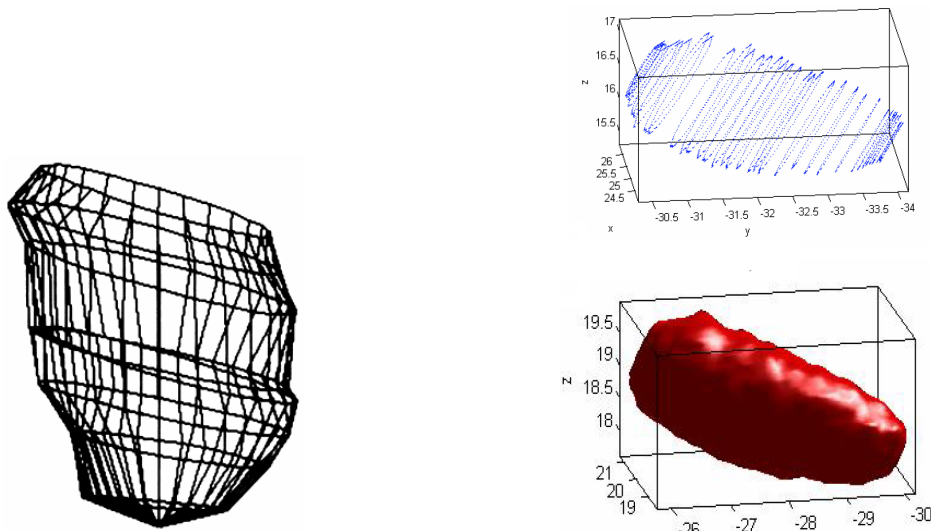
Figure 2.4: An overview of various geometric models evaluated in the work by Weijer *et al.* [5]. The full volume dataset (FV) is the "gold standard" reference dataset that was assembled from LV short-axis slices of the full LV blood pool. Both the hemisphere cylinder (HC) and biplane ellipsoid (BP) correlated better to the reference FV dataset than single-plane ellipsoid (SP) and modified Teichholz (TF) models. Modified Simpson (SR) model, as the only clinically recommended method for LV volume estimation, correlates the best with the reference FV dataset.

2.3 3D Reconstruction of LV Geometry

Work around three-dimensional (3D) reconstruction of the LV from 2D echocardiography is relatively limited compared to that around 3D echocardiography or other imaging modalities. Existing work share commonality in that cross-sectional images of the LV are acquired in multiple views and they are combined in a certain fashion. An early work that involved an *in vitro* study of the heart proposed a method that requires manual tracing of the endocardial borders in 10 short axis images and aligning them to form a reconstructed volume

2.3. 3D Reconstruction of LV Geometry

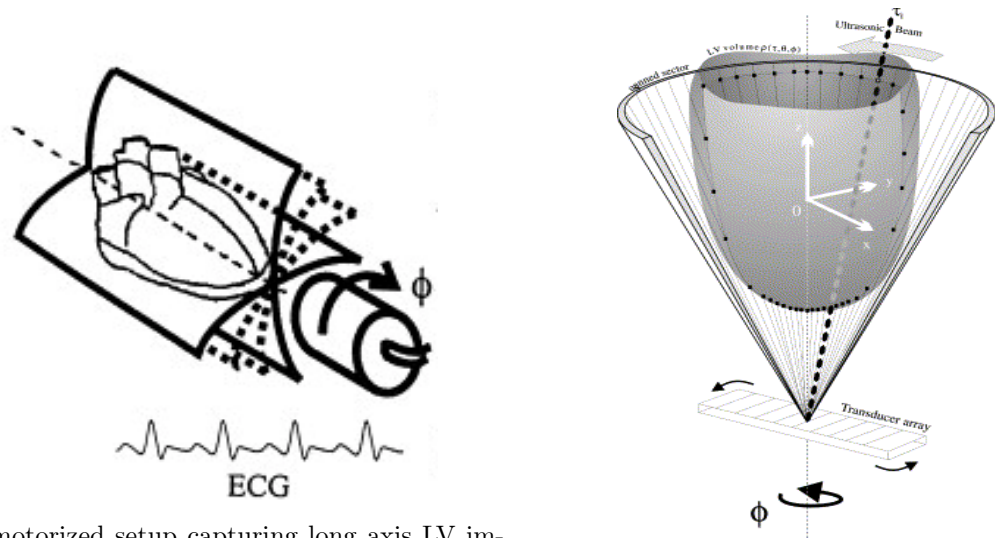
with triangular meshes fulfilling the LV surface [27]. A more recent attempt [28] was made to similarly capturing US images along the LV short axis but with much finer increments. Consequently, a smaller gap separates two cross-sectional LV endocardial traces. The surface area was interpolated using gradient vector flow method [29].



(a) Triangular LV surface interpolation. (b) Gradient vector flow LV surface interpolation.

Figure 2.5: LV volume 3D reconstruction from short axis images.

In contrast to obtaining endocardial borders from short axis images, another school of 3D LV volume reconstruction gathers endocardial border geometries from long axis images. Bonciu et al. [30] proposed a method that uses a motorized set up to rotate the US transducer to acquire numerous LV long axis image in fine angular intervals. The LV endocardial boundary surface was constructed by circular Shannon interpolation [31]. In a review that focuses on 3D echocardiography [32], it gathers that only 4 to 6 cross-sectional images are sufficient for optimal 3D reconstruction of the LV volume. There is work done to utilize machine learning models to infer the LV shapes from 2D US images [33]. Since machine learning is outside of the scope of this work, it will not be elaborated on.



(a) A motorized setup capturing long axis LV images.

(b) Gradient vector flow LV surface interpolation.

Figure 2.6: LV volume 3D reconstruction from long axis images.

2.4 Statistical Shape Models

Cardiac malfunction can also alter the physiological features of the LV geometry. For instance, the LV apex is usually stationary during a cardiac cycle for a healthy heart, but it would contract and extend during a cardiac cycle in a heart with medical conditions. Such a variation poses greater challenge for us to generalize the LV shapes, yet approaches leveraging on the statistical shape model (SSM) by [34], [35], and [36] attempt to provide a more realistic approximations of the LV geometry. Typically with the existing SSM approaches, a sufficiently large amount of training data consisting of varying LV geometries is assembled into a statistical model to encompass the variations of the LV geometries among the training population. The SSM can then be used to calculate how an incoming LV geometry deviates from the mean LV shape. This approach is often used to detect anomalies in the incoming LV as indicators for certain cardiac conditions or physiological changes post treatment. The accuracy of the SSM-based LV modeling benefits greatly from large amount of training data to capture more dimensional and geometric variations. Further, accurate calculation of the shape variation of an incoming LV shape requires considering all modes of variations of the SSM. However, data is often difficult to acquire in a research project and computational power is limited. Hence,

principle component analysis (PCA) is a common approach to reduce the dimensionality of the model [37, 38, 39, 40]. Nevertheless, as researchers pointed out, only the top few principal components contribute significantly to describing the modes of variations in a SSM. As such, in this work, we will describe the construction of an LV SSM and its use to estimate the LV blood pool volume and LVEF of a new, incoming patient dataset based on the training data and the n-most dominant principal models of variation featured in the training data.

Chapter 3

Methodology

3.1 Data Preparation

For this project, our clinical collaborator provided a set of tri-plane US images for 66 patients. All images were de-identified and the LV blood pool was manually traced in both diastole and systole images. In the sequence of tri-plane images for each patient, there is a US image taken at end-systole and one acquired at end-diastole. The three imaging planes correspond to the apical 2-chamber(2C) view, apical 3-chamber(3C) view, and apical 4-chamber(4C) view. Occasionally, the parasternal long-axis(PLAX) view replaces the 3C view when there were difficulties capturing images at 3C orientation on a patient. Moreover, these three imaging planes are roughly at 60 degrees relative to one another about the LV long axis, assuming correct image acquisition.

The PLAX view is obtained when the US wave slices through the long axis of the heart, which connects the base to the apex of the heart [41]. The apical 4C view is obtained at an orientation where all four chambers and the mitral valve of the heart are visible. The apical 2C view is obtained by rotating the US transducer 90 degrees clockwise from the 4C view. In the 2C view, the left ventricle, the left atrium, and the mitral valve should be visible. The apical 3C view should display the left ventricle, the left atrium, and the aortic valve, which are the same set of features visible in PLAX view.

After obtaining the clinical US image data set from our collaborator, we manually extracted

the LV blood pool areas (Figure 3.1 and Figure 3.2) in each US image where the collaborator already annotated the LV endocardial borders at end-diastole and end-systole with dotted lines of different colors. Our collaborator used the US images as underlay and determined the approximated LV blood pool boundaries based on his expertise and experience.

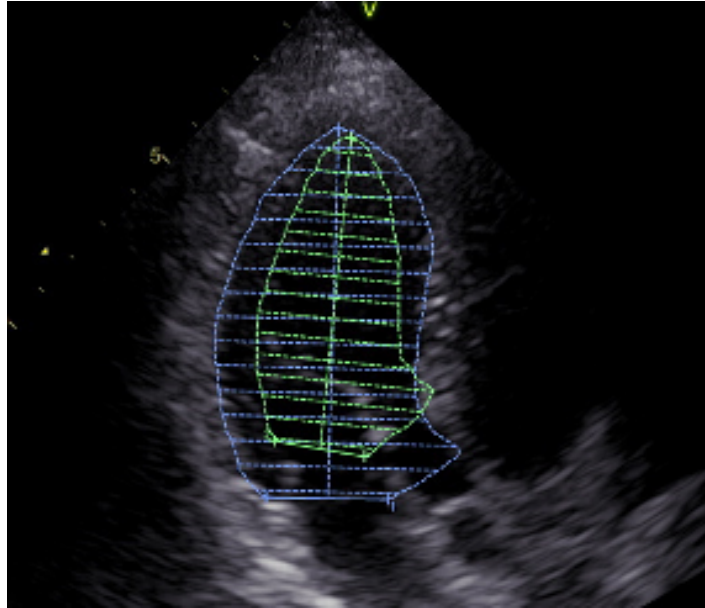
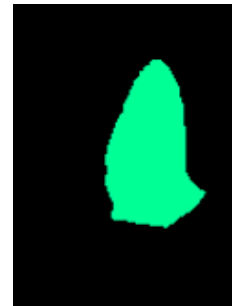


Figure 3.1: The zoomed-in section of the Figure 2.2 in which the LV blood pools at end-diastole and end-systole were traced by the clinical expert in blue and green, respectively.



(a) Manually segmented LV blood pool from Figure 3.1 at end-diastole.



(b) Manually segmented LV blood pool from Figure 3.1 at end-systole.

Figure 3.2: Manually segmented LV blood pools in end-diastole (ED) and end-systole (ES) from the patient-specific US images.

The manually extracted LV blood pool from each of the three tri-plane images were

3.2. Geometric Models Analysis

recorded for each patient so that their areas and geometries can be used for later analysis. Furthermore, the information generated by the software with which the clinical US scanners are equipped, GE EchoPac PC, that were displayed in the legend box of each US image were recorded. In the legend box (Figure 3.3), the rest time between each cardiac cycle ("R-R") and the heart rate ("HR") were displayed. For both the systolic and diastolic LV blood pools, the length ("L"), circumference ("C"), area ("A"), volume by area times length ("Va-l"), and volume by Method of Discs ("Vmod") were displayed in the legend box as well. For later analysis, we recorded the systolic and diastolic areas as well as the Method of Discs volumes for each image.



| | | |
|---|------|-----------------------|
| 3 | R-R | 890.83 ms |
| | HR | 67.35 BPM |
| 2 | L | 6.72 cm |
| | C | 16.32 cm |
| | A | 12.63 cm ² |
| | Va-l | 20.2 ml |
| | Vmod | 19.8 ml |
| 1 | L | 7.80 cm |
| | C | 20.70 cm |
| | A | 25.10 cm ² |
| | Va-l | 68.6 ml |
| | Vmod | 69.3 ml |

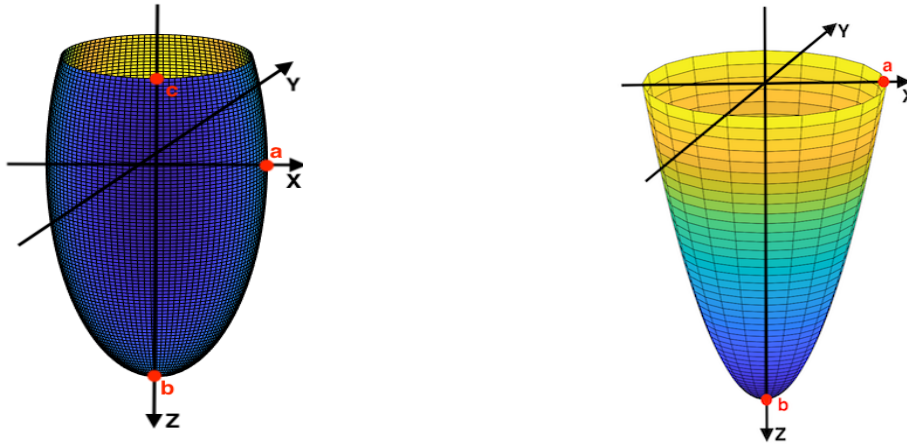
Figure 3.3: The zoomed-in section of the Figure 2.2 in which information related to the LV blood pools at end-diastole and end-systole were generated by the clinical US machine and displayed in the legend box at top left corner of the image.

3.2 Geometric Models Analysis

We first used mathematical models of the idealized LV geometry to study the difference between area and volume estimates of LVEF. Researchers previously proposed several mathemat-

3.2. Geometric Models Analysis

ical approximations of the LV geometry: cylindrical [24], truncated prolate spheroid (TPS) [4], and paraboloid [26] models. Of these, the TPS and paraboloid models matched more closely to the LV shapes observed in our US imaging data, so they were used for geometric simulations to characterize and describe the LV. Both models are characterized by the length and width of the LV in systole and diastole according to clinical knowledge about the heart size available from our US imaging data.



(a) The TPS model is described by three parameters, which measure the width \mathbf{a} at semi-axis \mathbf{x} , and lengths \mathbf{b} , \mathbf{c} from axis \mathbf{x} to the apex and the mitral valve base, respectively.

(b) A paraboloid model of the LV is characterized by two parameters descriptive of the length \mathbf{b} from semi-axis \mathbf{x} to the apex and width at semi-axis \mathbf{x} .

Figure 3.4: Mathematical approximations of the LV geometry using a truncated prolate spheroid (TPS) model and a paraboloid model.

As illustrated by Figure 3.4, TPS model is characterized by three parameters and the paraboloid model is characterized by two parameters. For the TPS model, parameter \mathbf{a} defines the shorter x-axis domain, parameter \mathbf{b} defines the longer z-axis domain, and parameter \mathbf{c} defines the location along z-axis where the ellipsoid is truncated. Similarly, the paraboloid model takes the same parameters \mathbf{a} and \mathbf{b} but not \mathbf{c} . The truncated section of the TPS model leads to significantly different cross-sectional areas and internal volumes from those described by the paraboloid for any given dimension. Using the information gathered from our image dataset, we ran simulations using the TPS and paraboloid models to generate shapes that range from thin-elongated LVs to wide-short LVs in order to cover a variety of

LV shapes. The corresponding LVEFs were calculated based on the simulated LV areas and volumes consequently.

3.3 3D Reconstruction

In the clinic, the software tool used by the clinicians estimates a LV blood pool volume using the Method of Discs from each of the three views in which the endocardial LV border was traced. In short, the method assumes that the left ventricle is axisymmetric about its long axis and approximates its volume by revolving each endocardial trace about the normal line connecting the apex to the midpoint of the mitral valve line. Moreover, to account for the fact that the heart was depicted using three views positioned at more or less 60 degrees apart, the same axisymmetric volume is estimated from the other two views in both systole and diastole. Finally, a systolic and diastolic blood pool volume is estimated by averaging the three volumes approximated from each of the three axisymmetrically-assumed views (refer to Figure 3.5).

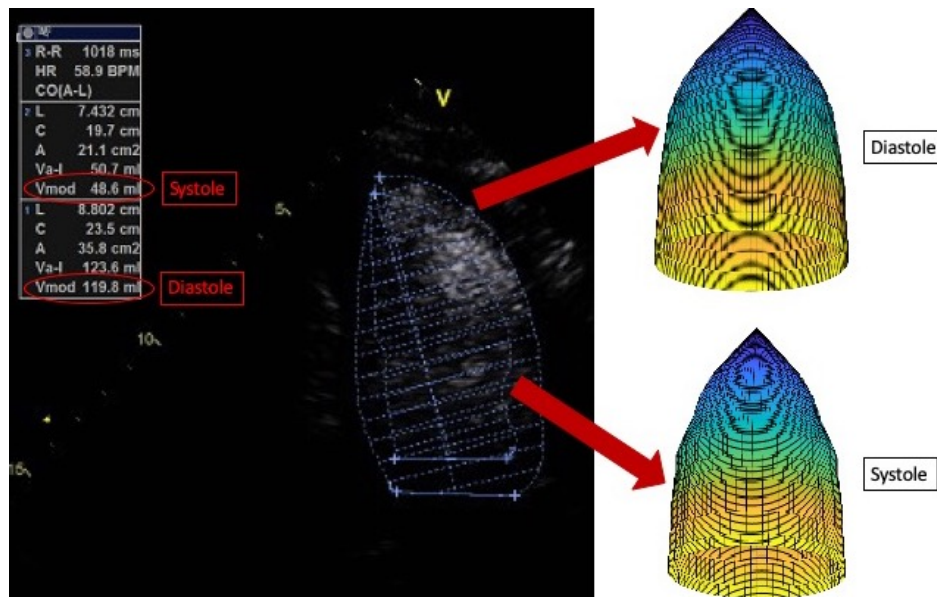


Figure 3.5: An illustration of systolic and diastolic LV volume estimation by the GE EchoPac clinical software using the Method of Discs by assuming that LV geometry is asymmetrical.

As an alternative method, which does not make any assumption about the LV axisymmetry, we proposed a method that leverages the true geometry of the LV depicted by the three 2D

multi-plane US images and their relative spatial location. As such, since each patient’s heart was imaged in three tomographic views located 60° apart, a 3D LV volume was reconstructed by first co-locating the LV apex from all views, then aligning the apex to mitral valve base line from the three views along the vertical axis, and lastly using using spline interpolation to connect points on the endocardial trace of the LV blood pool from each of the three views at the same elevation from the LV apex. This algorithm is similar to the one proposed by Dangi *et al.* [42], but differs by using the convex hull interpolation rather than the spline interpolation.

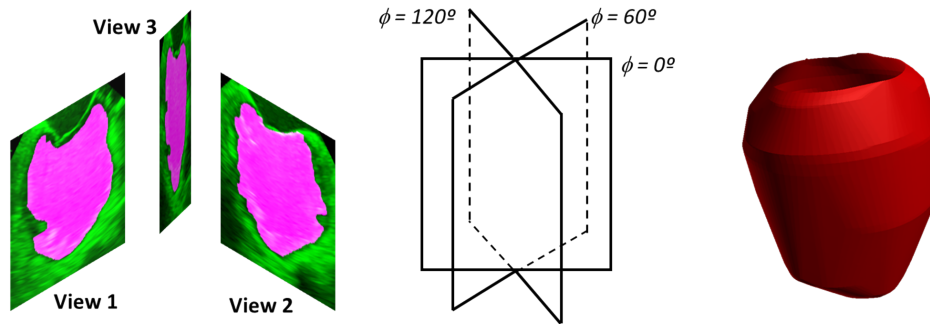


Figure 3.6: 3D reconstruction workflow: extract LV blood pools in three views; align apices and mitral valve bases; reconstruction by convex hull interpolation between three views.

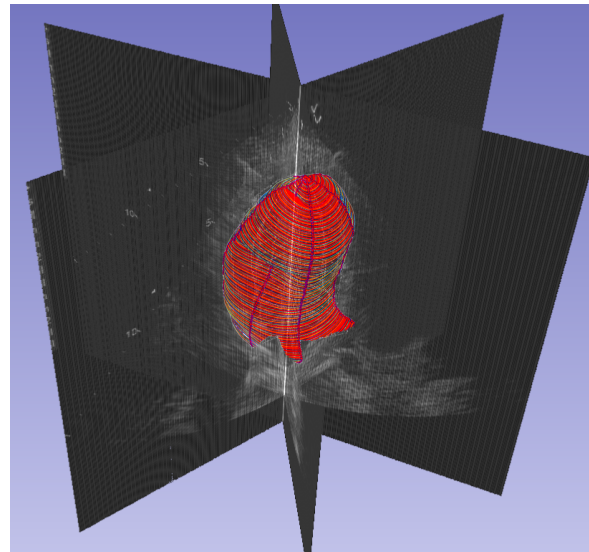


Figure 3.7: 3D Reconstruction of LV volume using convex hull model.

3.4 Statistical Shape Model

Executing the entire 3D reconstruction algorithm is time consuming and labor intensive due to the need for a clinical expert to manually extract the LV endocardial border and running the computationally intense reconstruction algorithm. Consequently, it is unattractive for clinicians to utilize this algorithm in real-time. The downside of the current practice poses a daring need for a method to more efficiently calculate LVEF based on volumetric data. To address these challenges, we propose a SSM-based estimation method that leverages on Mahalanobis distance or vector distance in the space spanned by the principal components (PC) of the training data. The SSM is assembled with landmarks that represent LV blood pool volume characteristics. For each tomographic view in the tri-plane image set, five anchor points were selected by the user. The five anchor points are located at five landmarks of the LV endocardial border: apex, mitral valve hinges, and midpoints of the endocardial wall on each side. The LV apex remains stationary during a cardiac cycle, so only one unique set of coordinates exists for the apex in all three views. which resulted in a total of 13 anchor points describing each dataset. Of the 66 patient-specific image datasets, we used 50 image datasets to build and train data the SSM, and the remaining 16 datasets were used as testing data. The shapes characterized by the 13 anchor points, Method of Discs volumes, and 3D reconstructed volumes of the 50 training data were used to predict the volumes and LVEFs of the 16 test datasets.

The 3D LV blood pool geometry of each patient consisted of a set of 13 anchor landmarks in systole and the same in diastole, while the SSM LV geometry consisted of 50 x 13 anchor landmarks in systole and same in diastole. Even though the anchor points were selected from 2D images, their transposition into the corresponding 3D volume was obtained under the clinically supported premise that the tri-plane 2D images were collected at 60 degrees apart. Using the reconstruction algorithm described in Section 3.3, all 2D anchor points were transformed into the 3D space. The coordinates of 3D-transformed landmarks are structured as detailed in Equation 3.4.1.

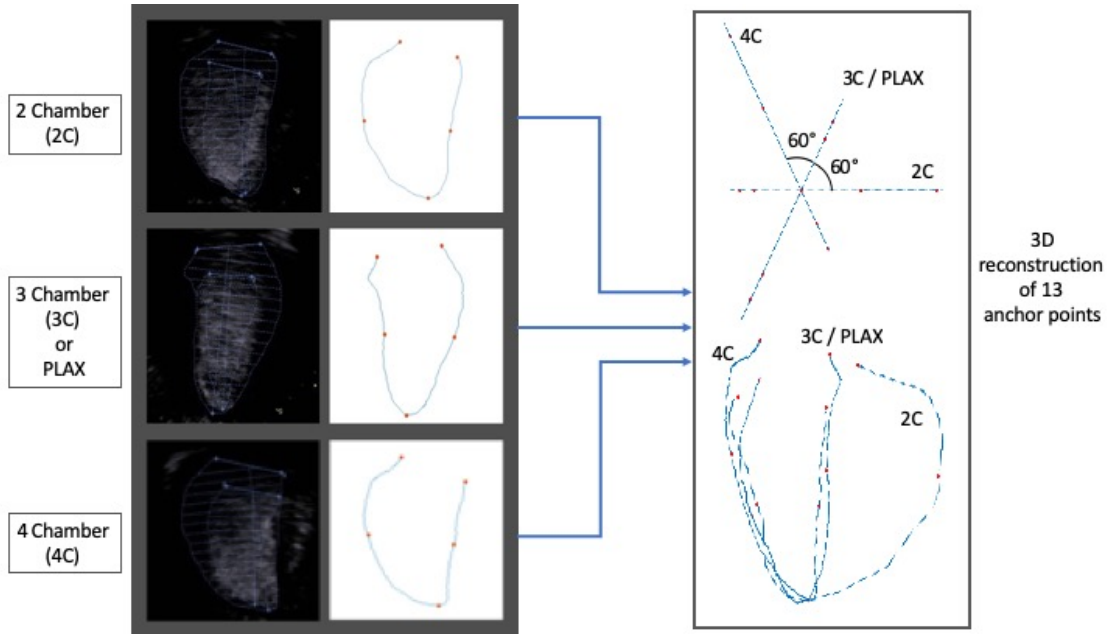


Figure 3.8: Anchor point locations on an example diastolic LV endocardial border (the outermost blue trace in the images with black background in the left column).

$$\text{Anchors}_{3D} = \begin{bmatrix}
 X_{left\ hinge-2C} & Y_{left\ hinge-2C} & Z_{left\ hinge-2C} \\
 X_{left\ mid-2C} & Y_{left\ mid-2C} & Z_{left\ mid-2C} \\
 X_{apex} & Y_{apex} & Z_{apex} \\
 X_{right\ mid-2C} & Y_{right\ mid-2C} & Z_{right\ mid-2C} \\
 X_{right\ hinge-2C} & Y_{right\ hinge-2C} & Z_{right\ hinge-2C} \\
 X_{left\ hinge-3C/PLAX} & Y_{left\ hinge-3C/PLAX} & Z_{left\ hinge-3C/PLAX} \\
 X_{left\ mid-3C/PLAX} & Y_{left\ mid-3C/PLAX} & Z_{left\ mid-3C/PLAX} \\
 X_{right\ mid-3C/PLAX} & Y_{right\ mid-3C/PLAX} & Z_{right\ mid-3C/PLAX} \\
 X_{right\ hinge-3C/PLAX} & Y_{right\ hinge-3C/PLAX} & Z_{right\ hinge-3C/PLAX} \\
 X_{left\ hinge-4C} & Y_{left\ hinge-4C} & Z_{left\ hinge-4C} \\
 X_{left\ mid-4C} & Y_{left\ mid-4C} & Z_{left\ mid-4C} \\
 X_{right\ mid-4C} & Y_{right\ mid-4C} & Z_{right\ mid-4C} \\
 X_{right\ hinge-4C} & Y_{right\ hinge-4C} & Z_{right\ hinge-4C}
 \end{bmatrix} = [13 \times 3] \tag{3.4.1}$$

For each landmark, there are X, Y, and Z coordinates. The subscripts describe which landmark each coordinate correspond to. "Left hinge" refers to the mitral valve hinge on the left side of the endocardial contour, "left mid" refers to the midpoint of the left half of the endocardial contour, and "apex" refers to the generally stationary apex of the left ventricle. Both the "right hinge" and "right mid" refer to the landmarks on the right side of the endocardial contour. "2C", "3C/PLAX", and "4C" refer to which tomographic view the coordinate represents. Since there is only one unique apex for the left ventricle, only one set of coordinates is used to represent the apex location.

The 3D coordinates of the 13 landmarks for the 50 training datasets were assembled into the SSM of dimension 50 x 13 x 3. Encompassing the landmark coordinates from all 50 training datasets is a prerequisite for constructing the SSM. LV shapes vary in size, so the alignment scheme was carefully determined. Since we will examine the LV volume estimation performances with and without size normalization, it was decided not to scale the training LV shapes based on their sizes while aligning them. The axis along which the three tomographic views intersect for each training patient image dataset was used as the alignment axis when combining the 50 datasets into the SSM. Once the landmarks of the 50 training datasets were aligned along the axis, their centers of mass along the alignment axis were calculated and offset to the origin, hence ensuring that the centroid of the SSM coincides with the origin. Finally, the centers of mass of all 50 LV shapes are also located at the origin, hence, (0, 0, 0) in 3D. The SSM is now ready to be used for LV volume estimations.

3.4.1 Mahalanobis Distance with Size Normalization

Once the SSM was generated, it was used to estimate the systolic and diastolic volumes of an incoming test patient. We used the inverse co-variance matrix of the SSM to calculate the Mahalanobis distance [43] between the test data and each of the training data in the SSM. The Mahalanobis distance can be calculated as defined below:

$$M_i = \sqrt{(test - train_i)^T C^{-1} (test - train_i)} \quad (3.4.2)$$

M_i is the Mahalanobis distance between a test dataset and each of the 50 training dataset with an index of i , C^{-1} is the inverse co-variance matrix of the SSM, and $()^T$ is the matrix transpose operation. Conceptually, the Mahalanobis distance describes how "far" a new dataset is from the training datasets. The Euclidean distance ($test - train_i$) between testing and training data in 3D space is calculated first, and its transpose is then multiplied by the co-variance matrix of the SSM, as well as the Euclidean distance.

The Mahalanobis distance between the test and each training dataset is used to calculate the weight according to which each training dataset contributes to the description of a new dataset. These weights were, in turn, used to estimate the systolic and diastolic volumes of the test dataset. As such, the larger the Mahalanobis distance from a test dataset to a training dataset, the lower the weight by which that specific training dataset contributes to describing the test dataset.

$$w_i = \frac{\sum_{i=0}^{50} M_i}{M_i} \quad (3.4.3)$$

Finally, both the systolic and diastolic volumes of the test dataset can be estimated using the calculated weights multiplied by the corresponding ground truth volumes of each training dataset.

$$V_{estimated} = \sum_{i=0}^{50} w_i V_i \quad (3.4.4)$$

3.4.2 Vector Distance without Size Normalization

As opposed to using the Mahalanobis distance which removes the effect of size differences in the LV shape due to normalization, we also employed an alternative, yet more traditional method to account for the size effect. The vector distance resulting from the dot product of the test patient's anchor points and each training patient's anchor points was used to determine the contributing weight of each training LV shape in the SSM for test patient LV volume estimations. To assist with the principal component analysis (PCA) in the later steps, the matrix containing all 50 training patients' 3D anchor points was first reshaped from 50 x 13 x

3 to 50 x 39.

$$A = 50 \times \begin{bmatrix} x_1 & y_1 & z_1 \\ x_2 & y_2 & z_2 \\ \vdots & \vdots & \vdots \\ x_{13} & y_{13} & z_{13} \end{bmatrix} \Rightarrow 50 \times \begin{bmatrix} x_1 \\ y_1 \\ z_1 \\ x_2 \\ y_2 \\ z_2 \\ \vdots \\ x_{13} \\ y_{13} \\ z_{13} \end{bmatrix} \quad (3.4.5)$$

Since obtaining real eigenvalues and eigenvectors requires the training patient anchor point matrix to be a symmetric matrix, we first computed the Gramian matrix as follows:

$$A' = [50 \times 39]^T [50 \times 39] = [39 \times 50] [50 \times 39] = [39 \times 39]. \quad (3.4.6)$$

Using the eigen-decomposition, the eigenvalues and eigenvectors of the SSM were calculated as shown in Equation 4, where $\underline{\lambda}$ is the diagonal matrix consisting of eigenvalues and \underline{D} is the matrix of corresponding eigenvectors.

$$\underline{A}' \underline{D} = \underline{\lambda} \underline{D} \quad (3.4.7)$$

The eigenvectors were sorted with respect to their corresponding eigenvalues in descending order, which allowed for PC dimensionality reduction in the subsequent steps of the analysis. All landmarks of the 66 patient datasets were projected onto the PC space via multiplication by the eigenvector matrix so that they are represented as a linear combination of the 39 modes of variation of the SSM. The vector distance in PC space P_i between a test patient and each training patient in PC space was calculated. The PCA vector distances were used to determine the weight w_i each training patient's LV volume V_i contributed to a new test

patient's LV volume estimate, as shown by Equations 3.4.8 and 3.4.9.

$$w_i = \frac{\sum_{i=0}^{50} M_i}{M_i} \text{ or } \frac{\sum_{i=0}^{50} P_i}{P_i} \quad (3.4.8)$$

$$V_{estimated} = \sum_{i=0}^{50} w_i V_i \quad (3.4.9)$$

The reference volume V_i of each patient is calculated as a linear combination of the LV volumes reconstructed using the algorithm explained in Section 3.3.

Chapter 4

Results

4.1 Geometric Model

As observed from the retrospectively acquired and de-identified image database of 66 patients, the diameters of LV blood pools ranged from 1 cm to 4 cm and the lengths ranged from 2 cm to 10 cm. LV cross-sectional areas and volumes in both systole and diastole and the corresponding LVEFs were calculated for both idealized models across the whole range of heart sizes and geometries. Comparing the area- vs. volume-based LVEFs, both models clearly demonstrate that the area-based LVEF is significantly lower than the volume-based LVEF by approximately 16% on average. Volume-based LVEFs are higher than area-based ones across the lengths and radii of the LVs used to run the TPS and paraboloid model simulations. Further, the differences between volume-based and area-based LVEFs are higher for thin-elongated LV shapes than for wide-short LV shapes using either geometric model. The Student's t test also confirmed that the area-based LVEF is significantly lower ($p < 0.05$) than the volume-based LVEF for all analyzed data.

Subsequently, the area- and volume-based LV measurements in both systole and diastole for our clinical data, TPS model, and paraboloid model were compared. As summarized in Table 4.1, the LVEF area and volume calculations are consistently different across all models. In all models, area-based LVEF calculations clearly underestimate the volume-based LVEF calculations for all models. Even though the mean and standard deviation of LVEFs based on

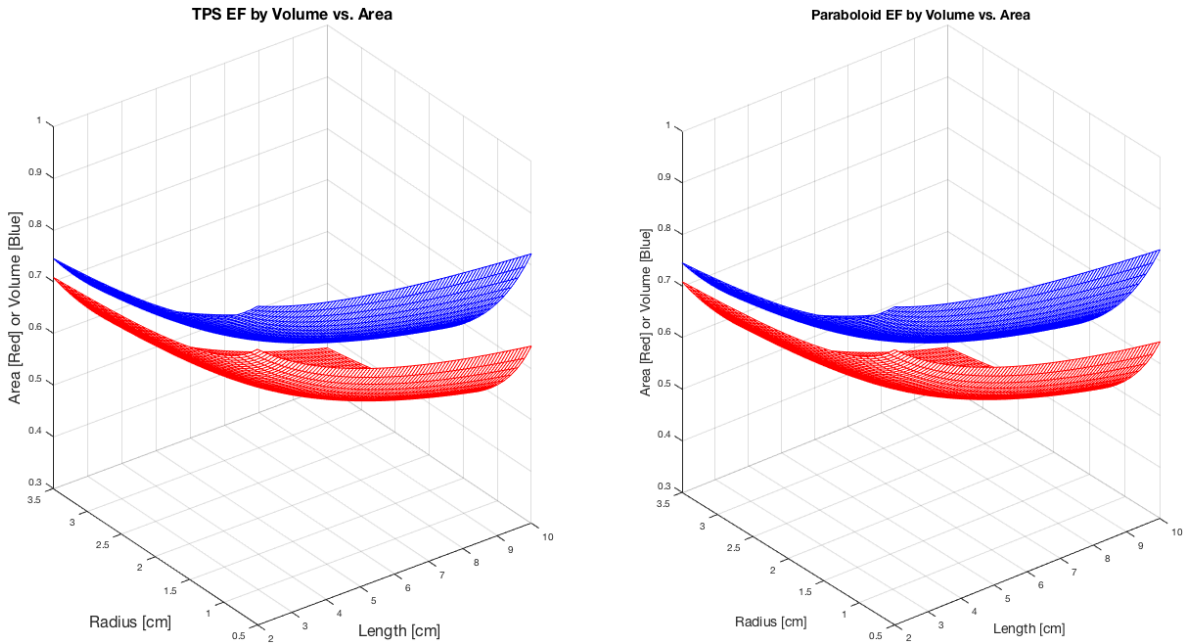


Figure 4.1: The difference of LVEFs calculated based on volume and area using TPS and paraboloid models.

TPS and paraboloid models were the same, both quantities were produced from significantly different stroke and diastolic areas or volumes as shown in Table 4.1.

Table 4.1: Summary statistics of the LVEF-related quantities based on the TPS model, paraboloid model, and the clinical data analyzed using GE’s EchoPac PC clinical software.

| Model | Mean±Standard Deviation | | | | | |
|------------|-------------------------|-----------------|-----------------|------------------|------------------|------------------|
| | LVEF | | Diastolic | | Stroke | |
| | Area [%] | Volume [%] | Area [cm^2] | Volume [ml] | Area [cm^2] | Volume [ml] |
| Image Data | 41.8 ± 12.7 | 58.7 ± 15.9 | 13.9 ± 4.1 | 67.4 ± 20.0 | 35.1 ± 9.7 | 126.8 ± 59.2 |
| TPS | 41.3 ± 4.7 | 55.4 ± 5.7 | 16.1 ± 2.3 | 99.5 ± 29.1 | 40.0 ± 10.1 | 186.9 ± 73.1 |
| Paraboloid | 41.3 ± 4.7 | 55.4 ± 5.7 | 17.3 ± 3.8 | 174.2 ± 35.4 | 42.67 ± 12.4 | 316.7 ± 89.0 |

Comparing the stroke and diastolic areas and volumes, the TPS model matched more closely to our reconstruction results from the US imaging data. The paraboloid model tends to overestimate the volume relative to the TPS model in the mid to apical range due to their different geometries. This observation also explains the limitations of using these idealized models to faithfully describe the LV geometry, but the TPS model is still considered a better

approximation of the LV shape. Additionally, due to imperfect extraction of the LV blood pool from our US images, the systolic areas and volumes were higher resulting in further reduction in LVEFs. Moreover, the volume-based values in the 'Clinical Data' column are not gold standard because they were calculated by the GE EchoPac PC clinical software using Method of Discs volume estimation method for each tomographic view without considering intricate variations in LV shapes between tomographic views.

4.2 3D LV Blood Pool Reconstruction

Since the 3D reconstruction serves as the basis for the SSM construction and the eventual PC analysis, it is necessary to validate the 3D reconstruction algorithm to ensure it matches sufficiently well or improves upon the reference MOD algorithm. The systolic and diastolic volumes of all 66 patients in the US image dataset were provided in the legend boxes shown in the US images. There are three tomographic views for each patient's images, the MOD volumes in all tomographic views were averaged (equation 2) for both end-systole and end-diastole to allow for the calculation of one LVEF per patient based on MOD volumes. On the other hand, one systolic volume and one diastolic volume were generated from the 3D reconstruction for each patient, so the LVEF was simply calculated from those volumes. The result summary is tabulated below to compare the systolic volumes, diastolic volumes, and their derived LVEFs based on MOD and 3D reconstruction.

Table 4.2: Statistics of the LVEF-related quantities based on the reference MOD and 3D blood pool reconstructions from the multi-plane 2D US imaging data.

| Mean \pm Standard Error* | MOD | 3D Reconstruction |
|----------------------------|-----------------|-------------------|
| LVEF [%] | 58.6 \pm 2.0 | 57.8 \pm 2.0 |
| Diastolic [ml] | 127.0 \pm 7.3 | 127.5 \pm 7.2 |
| Stroke [ml] | 67.3 \pm 2.5 | 66.8 \pm 2.4 |

$$Standard\ Error = Standard\ Deviation / \sqrt{Number\ of\ Samples} \quad (4.2.1)$$

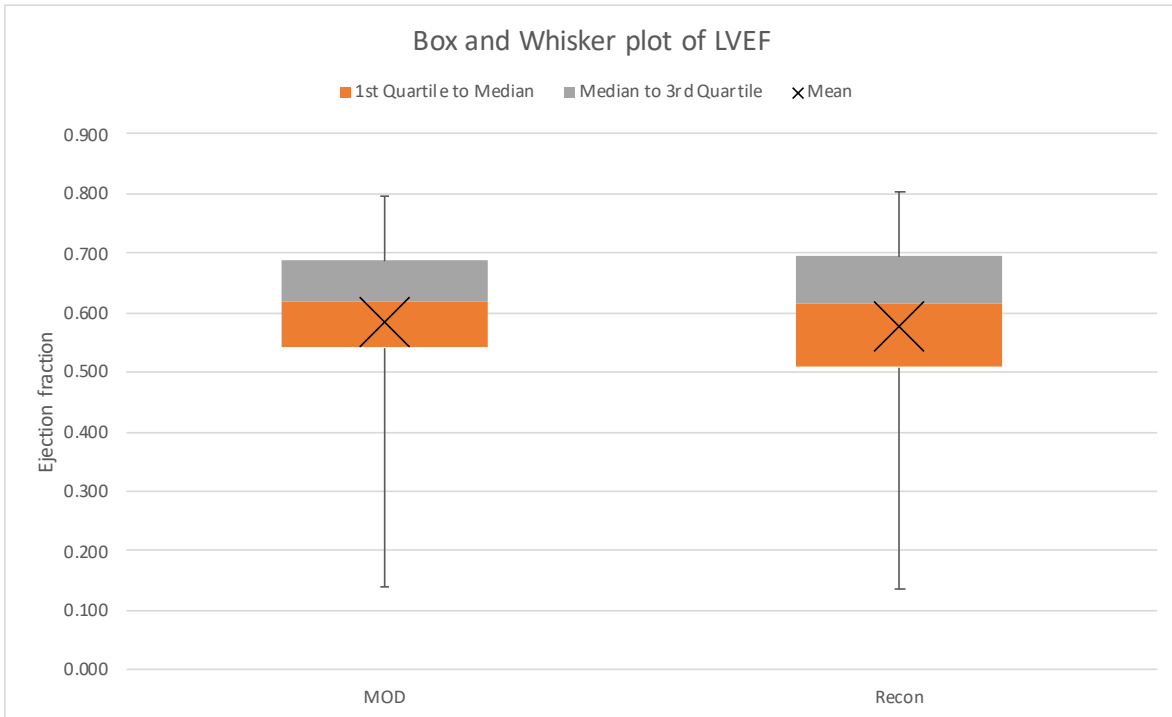


Figure 4.2: A box and whisker plot of the LVEF calculated from MOD and 3D reconstructed volumes.

As shown by Table 4.2, results from 3D reconstruction algorithms match closely to the reference MOD values. Even though the reconstructed LV volumes resemble an LV geometry more realistically, having only three tomographic views limits the accuracy improvement potential of the reconstructed volumes. Notwithstanding, the reconstruction algorithm is at least as good as the standard-of-care MOD volume estimations. Further, the LVEF results based on reconstruction algorithm were compared against the reference MOD values in Figure 4.3. If the two algorithms match perfectly, the resulting slope of the plot should be unity. In fact, the experimental results led to a slope of 0.97 and a coefficient of determination of 0.93, which confirms the reconstruction algorithm closely matches the performance of the reference MOD.

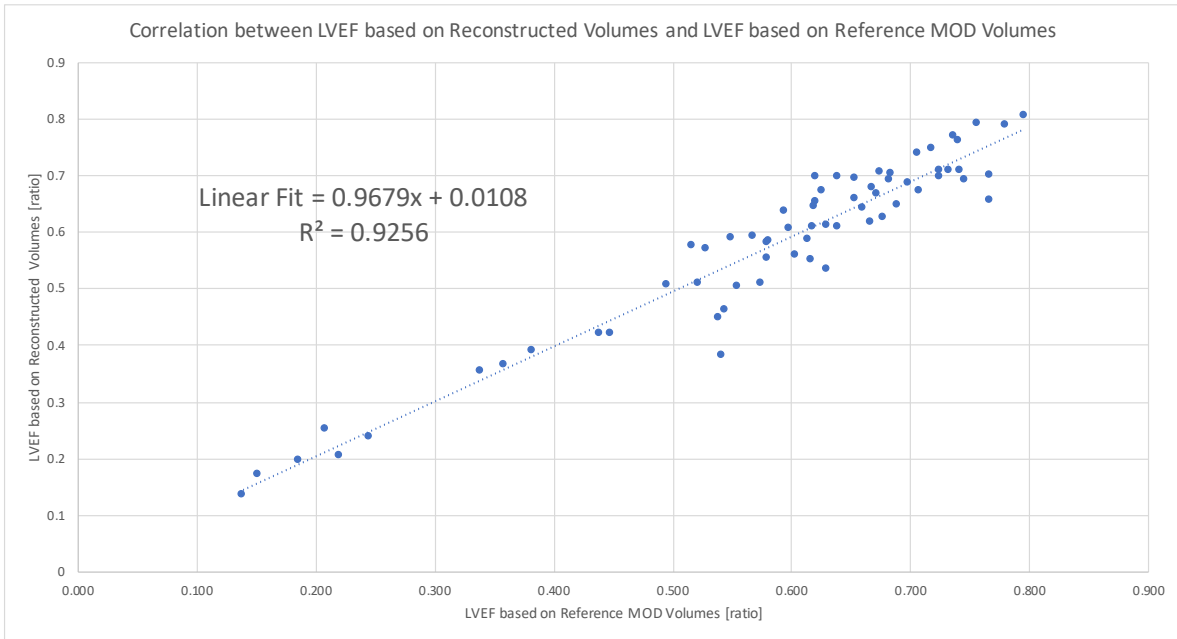


Figure 4.3: Plotting the LVEF results based on 3D reconstructed volumes to the reference MOD values provides a slope of 0.97 and a coefficient of determination of 0.93.

4.3 Statistical Shape Model

After confirming the 3D reconstruction algorithm is sufficiently accurate to estimate the LV blood pool volume, it was used in the next phase of the work to generate a statistical shape model (SSM) from 2D LV landmarks. LV landmarks from the 50 training patients were assembled into a point cloud that is the SSM, which encompasses the numerous LV geometries in the dataset. For each set of the 13 landmarks, its center of gravity along the central vertical axis was calculated and tared to the zero origin. All 50 sets of land marks centered at the origin would generate a zero-mean SSM as illustrated by Figure 4.4.

It is important to verify that the SSM can produce reasonably accurate LV volume estimations comparing to the reference data. Hence, a "take one out" method was employed to construct a SSM based on 49 training patients to estimate the volumes of the "left-out" training patient. Such process was repeated to estimate the LV blood pool volume in systole and diastole for each of the 50 training patients. The Bland-Altman plot in Figure 4.5 illustrates the agreement between SSM-derived LVEFs and the reference MOD LVEFs. Along the

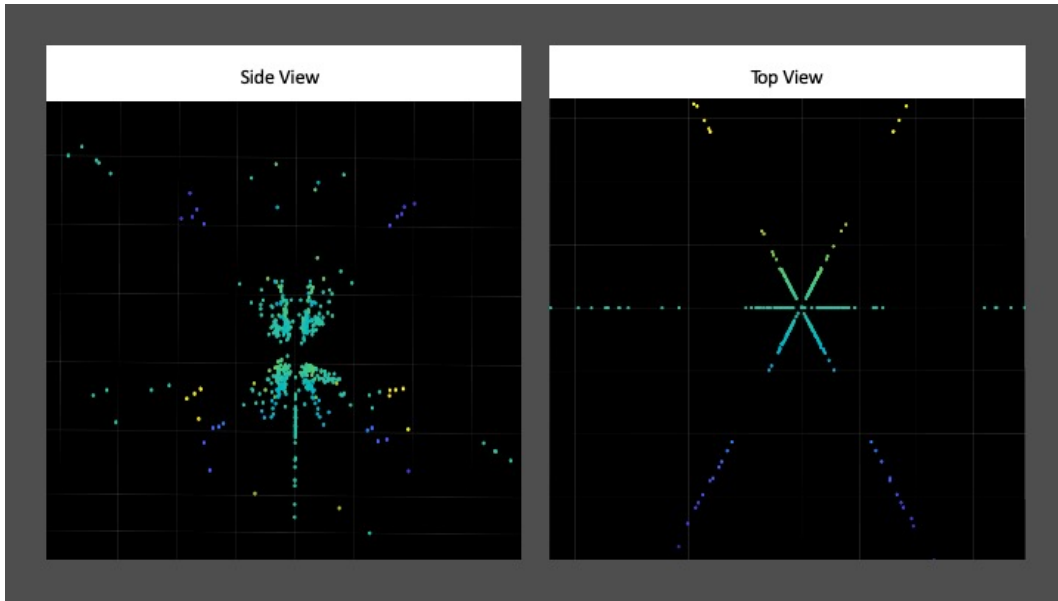


Figure 4.4: The point cloud constructed from land marks of the 50 training image datasets.

x axis are the means of the 50 pairs of SSM-derived LVEFs and the corresponding reference MOD-based LVEFs. Along the y axis are the differences between the SSM-derived LVEFs and MOD-based LVEFs. The red line across the plot illustrates the mean of the differences of all 50 pairs. The dark gray line above and the green line below the red line are the limits of agreement, which were set to 95% prediction interval which are 1.96 standard deviation apart from the mean. As Figure 4.5 illustrates, SSM-derived LVEFs agree strongly with the reference MOD LVEFs with only 10% data points outside of the limits of agreement.

For the 16 testing patient image datasets, their corresponding LV diastolic and systolic volumes were estimated from the reference MOD and 3D reconstructed values using both the Mahalanobis distance and the PC space vector distance. The percent error δ between either the MOD (Figures 4.6 - 4.8) or 3D reconstructed (Figures 4.9 - 4.11) reference value V_{ref} and the estimated value V_{est} was calculated for estimated systolic and diastolic volumes based on both the Mahalanobis and PC vector distances.

$$\delta = \left| \frac{V_{ref} - V_{est}}{V_{est}} \right| \cdot 100\% \quad (4.3.2)$$

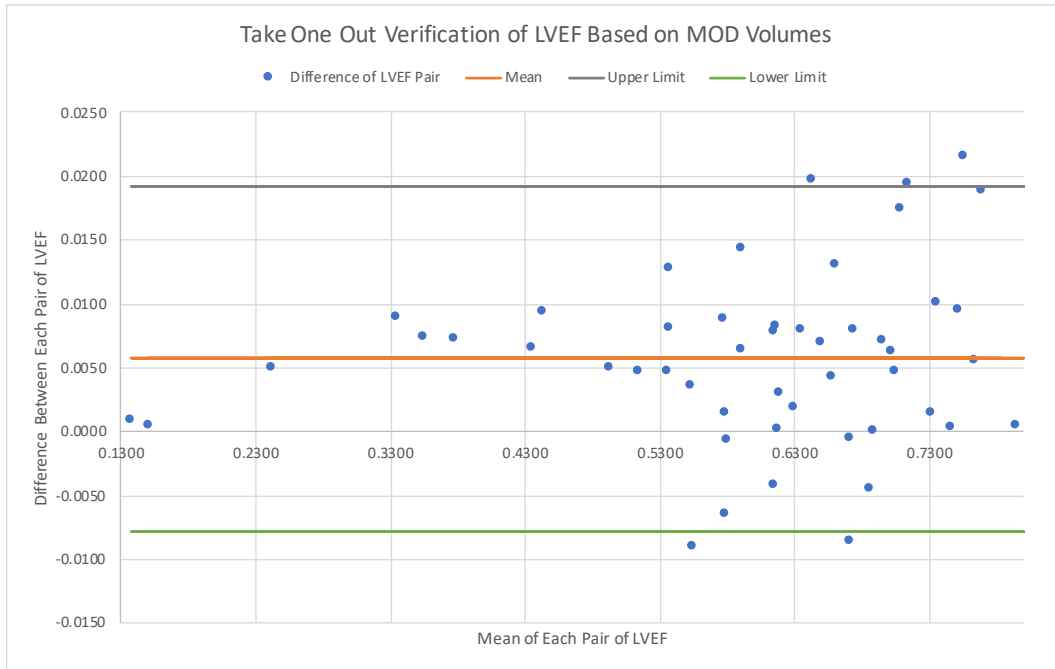


Figure 4.5: Bland-Altman plot of the SSM-derived LVEFs and the reference MOD LVEFs.

The results based on Mahalanobis distance were consistently further away from either the reference MOD data or the 3D reconstructed data than the results based on PC space vector distance. This observation indicates that size normalization is undesirable in estimating LV geometries due to the importance of the size to the volume estimation.

Table 4.3: Summary statistics of the LVEF-related estimates using the Mahalanobis distance and PC space vector distance based on the reference MOD values for the 16 testing patients.

| Mean \pm Standard Error | MOD | Mahalanobis Distance | PC Vector Distance |
|---------------------------|------------------|----------------------|--------------------|
| LVEF [%] | 55.7 \pm 4.7 | 48.9 \pm 4.3 | 57.4 \pm 5.0 |
| Diastolic Volume [ml] | 125.8 \pm 17.9 | 117.3 \pm 17.4 | 126.8 \pm 18.1 |
| Systolic Volume [ml] | 66.4 \pm 17.7 | 68.7 \pm 16.9 | 66.9 \pm 17.9 |

As a PC explains a mode of variation in the SSM, PCA was conducted to provide more insights on the effects various aspects of the SSM-based LV volume estimations pose on the overall accuracy. By sorting the eigenvalues and their corresponding eigenvectors in descending order, the eigenvectors or PCs that contribute the most to describing the LV geometry surfaced.

4.3. Statistical Shape Model

Table 4.4: Summary statistics of the LVEF-related estimates from the Mahalanobis distance and PC space vector distance based on the 3D reconstructed values for the 16 testing patients.

| Mean \pm Standard Error | Reconstruction | Mahalanobis Distance | PC Vector Distance |
|---------------------------|------------------|----------------------|--------------------|
| LVEF [%] | 55.6 \pm 2.2 | 58.5 \pm 2.5 | 54.5 \pm 2.3 |
| Diastolic Volume [ml] | 125.8 \pm 17.3 | 130.1 \pm 17.4 | 123.3 \pm 17.3 |
| Systolic Volume [ml] | 66.2 \pm 17.1 | 65.7 \pm 17.4 | 66.0 \pm 17.1 |

For each of the 16 testing patient datasets, the estimation error was plotted against the number of PCs utilized sorted in descending order of their corresponding eigenvalues. As illustrated by Figure 4.13, as the number of sorted PCs used to estimate LV volumes exceed approximately 13, the margin of return on accuracy improvement dramatically diminishes.

Since the first 13 PCs contribute to most of the LV volume estimation, a few reduced numbers of PCs for vector distance calculation were chosen to reduce the dimensionality of the SSM. Instead of using all 39 PCs, the three, five, and ten most dominant PCs were used to estimate LV volumes by vector distance. Note that even when using only the three or five most dominant PCs, the percent error between the estimated and true volumes was less than 10%, while using the most dominant ten PCs provides close estimation to the reference data with less than 5% error.

Table 4.5: Summary statistics of the LVEF-related quantities using reduced number of PCs to estimate for the 16 testing patients.

| Mean \pm Standard Error | Number of PCs | | | |
|---------------------------|------------------|--------------------|------------------|------------------|
| | 3 | 5 | 10 | 39 |
| LVEF [%] | 61.1 \pm 5.0 | 59.9 \pm 4.7 | 57.8 \pm 5.0 | 54.5 \pm 4.6 |
| LVEF Percent Error* [%] | 9.9 | 7.7 | 4.0 | 2.0 |
| Diastolic Volume [ml] | 118.1 \pm 17.4 | 119.7.1 \pm 17.2 | 122.3 \pm 17.3 | 123.3 \pm 17.3 |
| Systolic Volume [ml] | 56.8 \pm 17.3 | 57.9 \pm 15.7 | 62.7 \pm 17.8 | 66.0 \pm 17.1 |

$$PercentError = |Estimated LVEF - Image data LVEF| / Image data LVEF * 100\% \quad (4.3.3)$$

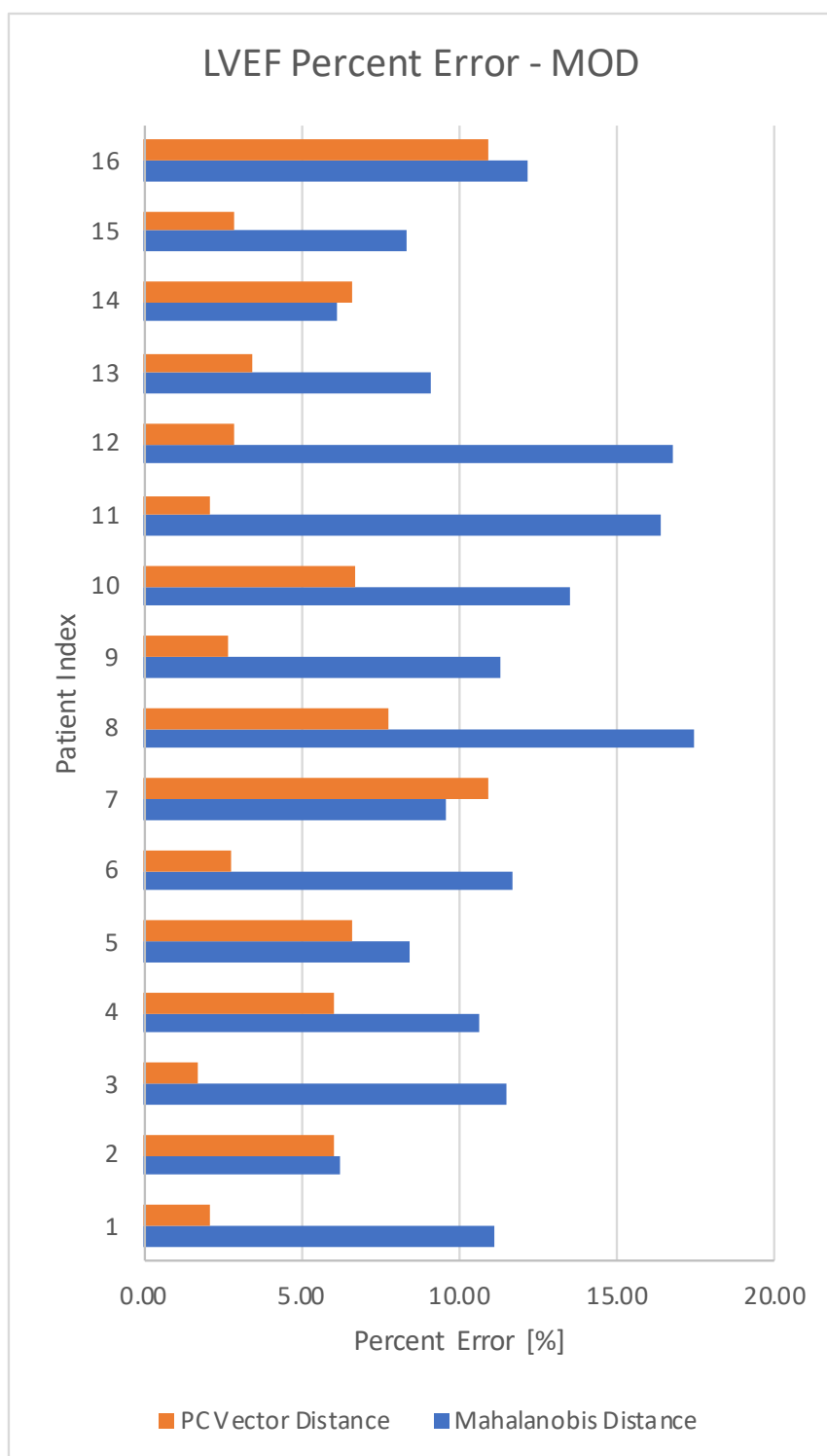


Figure 4.6: Patient-specific percent error of the estimated LVEF based on the reference MOD data using Mahalanobis distance and PC vector distance methods.

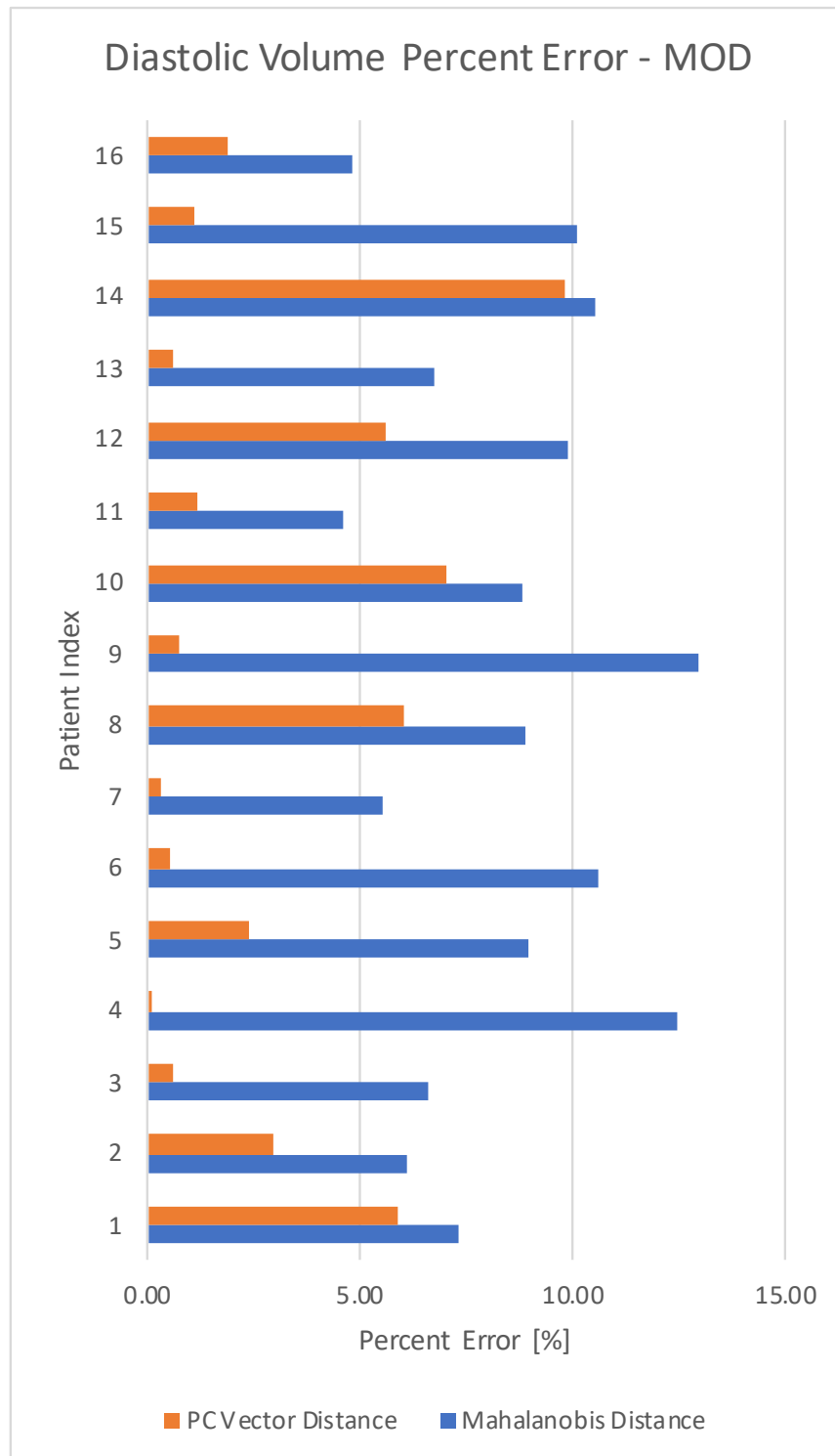


Figure 4.7: Patient-specific percent error of the estimated LVEF based on the reference MOD data using Mahalanobis distance and PC vector distance methods.

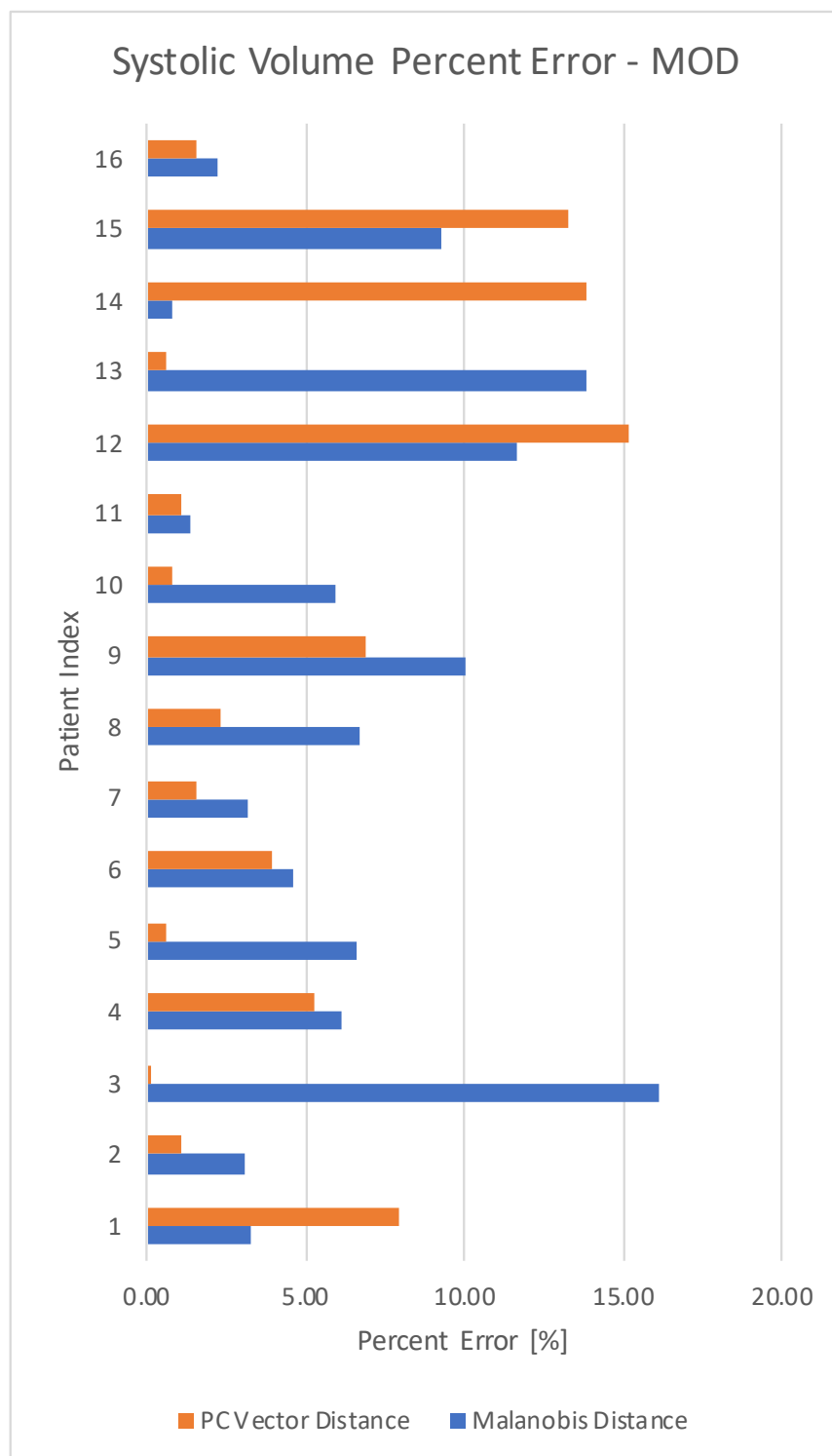


Figure 4.8: Patient-specific percent error of the estimated LVEF based on the reference MOD data using Mahalanobis distance and PC vector distance methods.

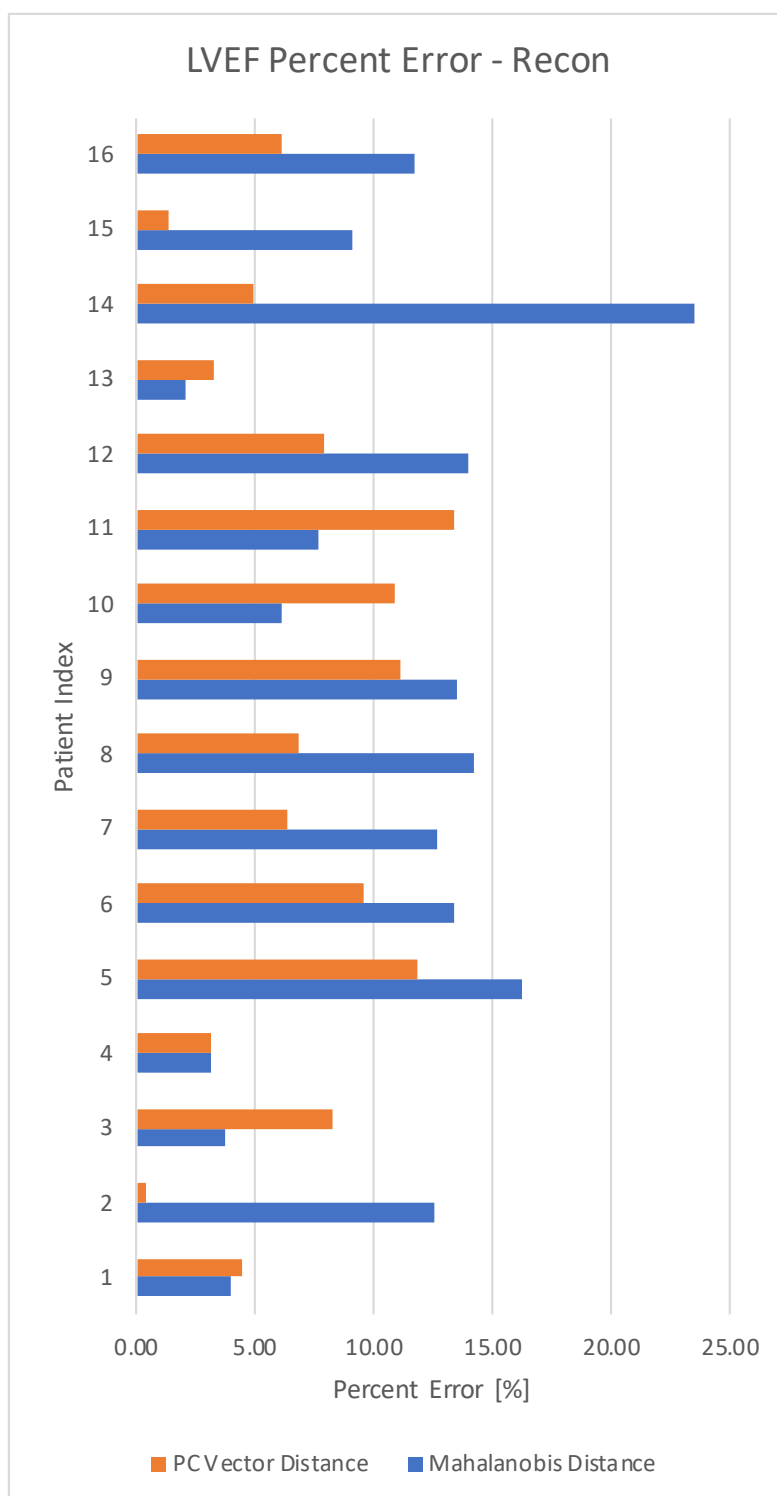


Figure 4.9: Patient-specific percent error of the estimated LVEF based on the 3D reconstruction data using Mahalanobis distance and PC vector distance methods.

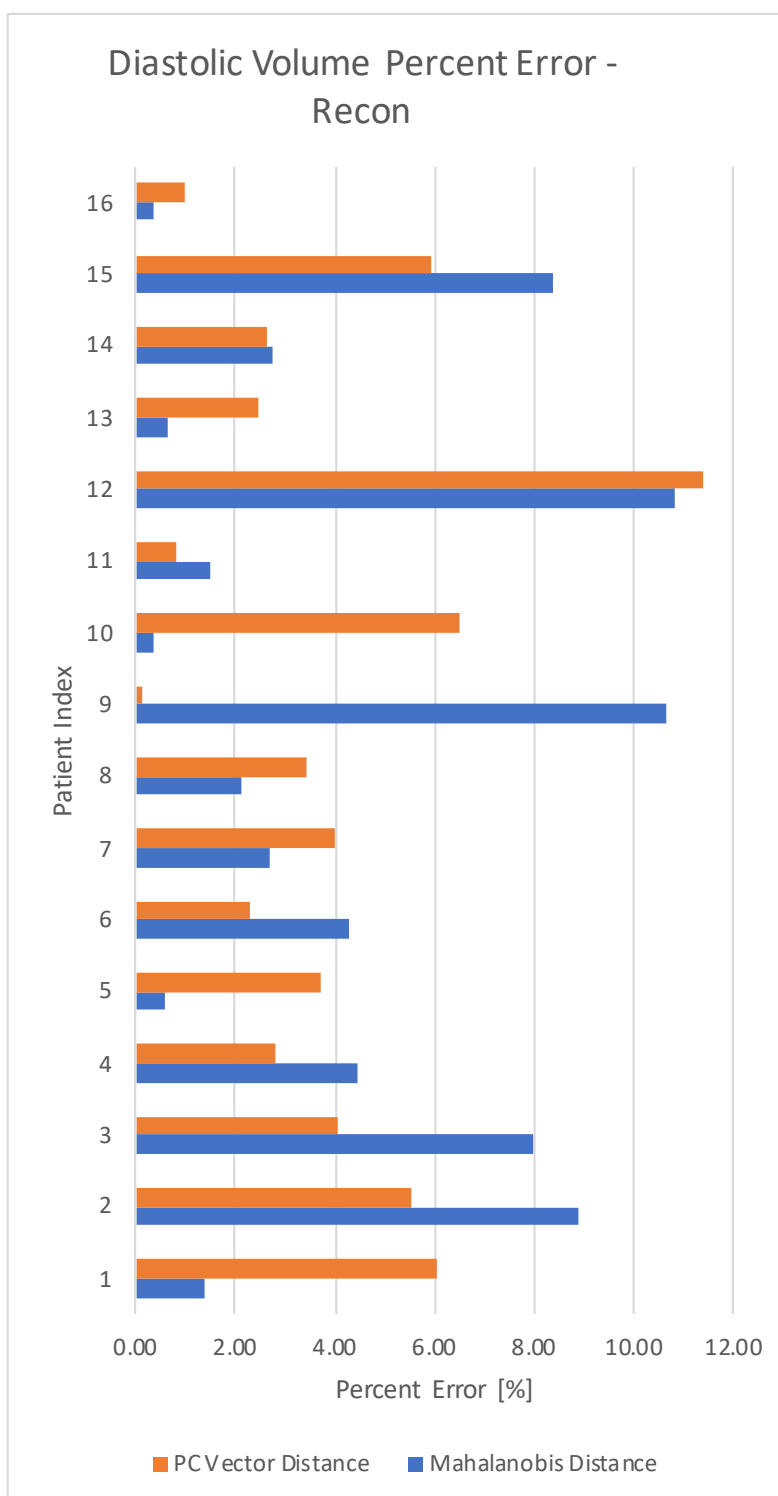


Figure 4.10: Patient-specific percent error of the estimated LVEF based on the 3D reconstruction data using Mahalanobis distance and PC vector distance methods.

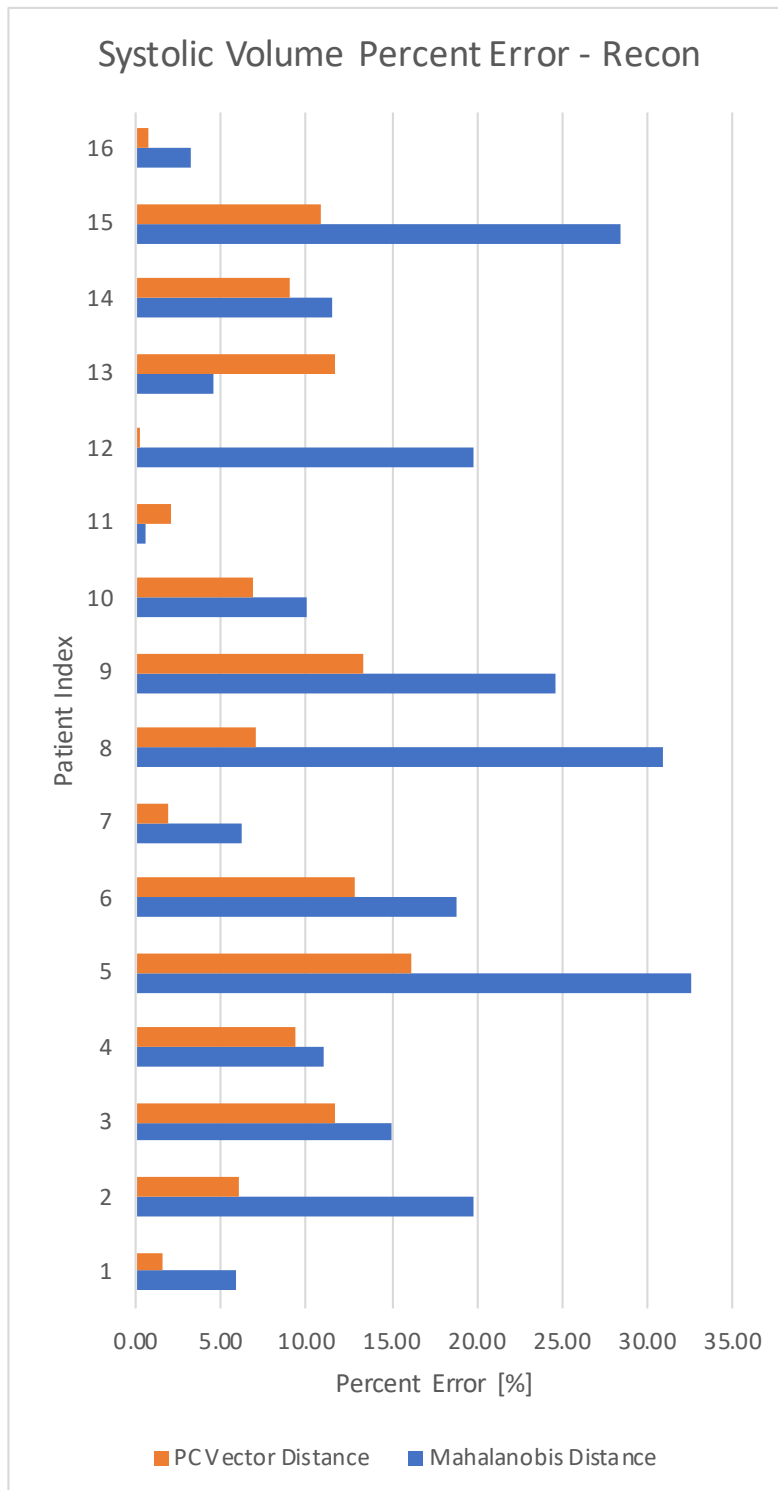


Figure 4.11: Patient-specific percent error of the estimated LVEF based on the 3D reconstruction data using Mahalanobis distance and PC vector distance methods.

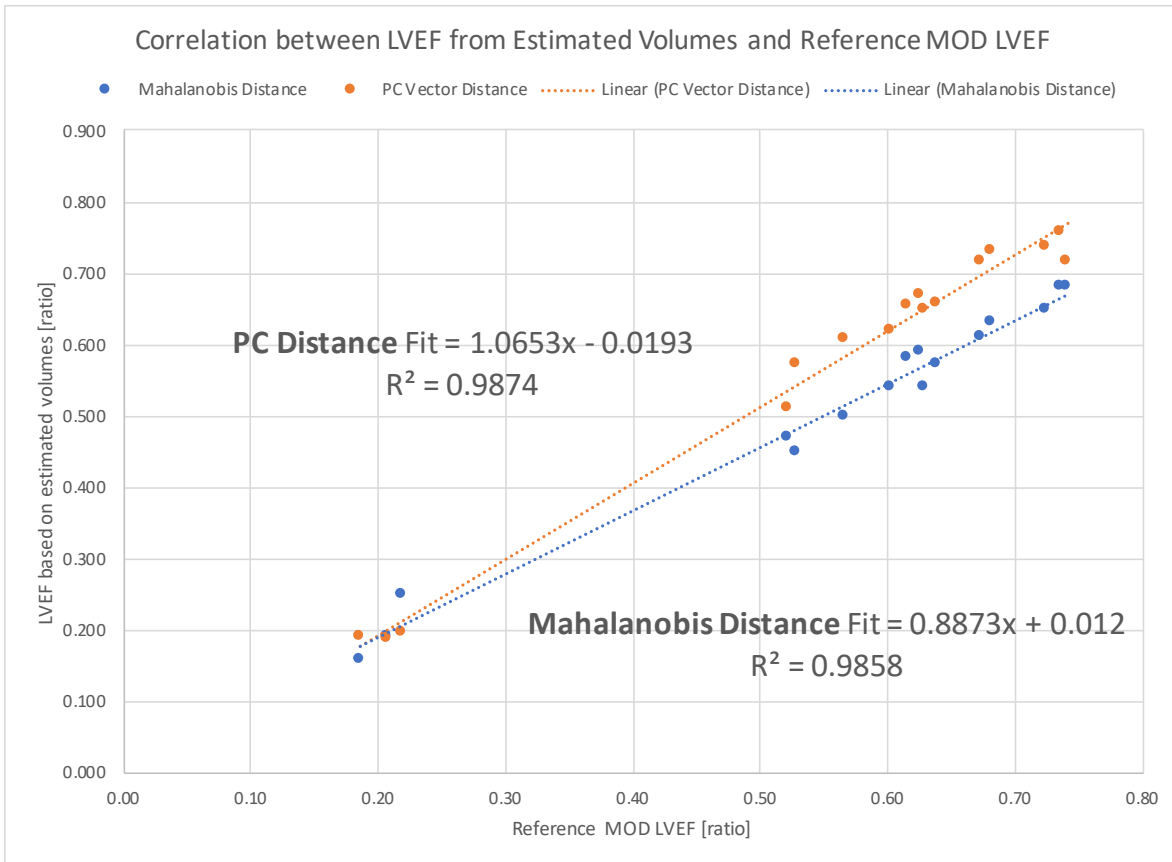


Figure 4.12: Plotting the LVEF results based on estimated systolic and diastolic volumes using Mahalanobis and PC Vector distances against the reference MOD values provides a linear fit of 0.887 for LVEF based on Mahalanobis distance and 1.065 for LVEF based on PC vector distance. The linear fit on the LVEF using PC vector distance is slightly better than that on the LVEF using Mahalanobis distance according to the coefficient of determination of 0.987 for the former versus 0.986 for the latter.

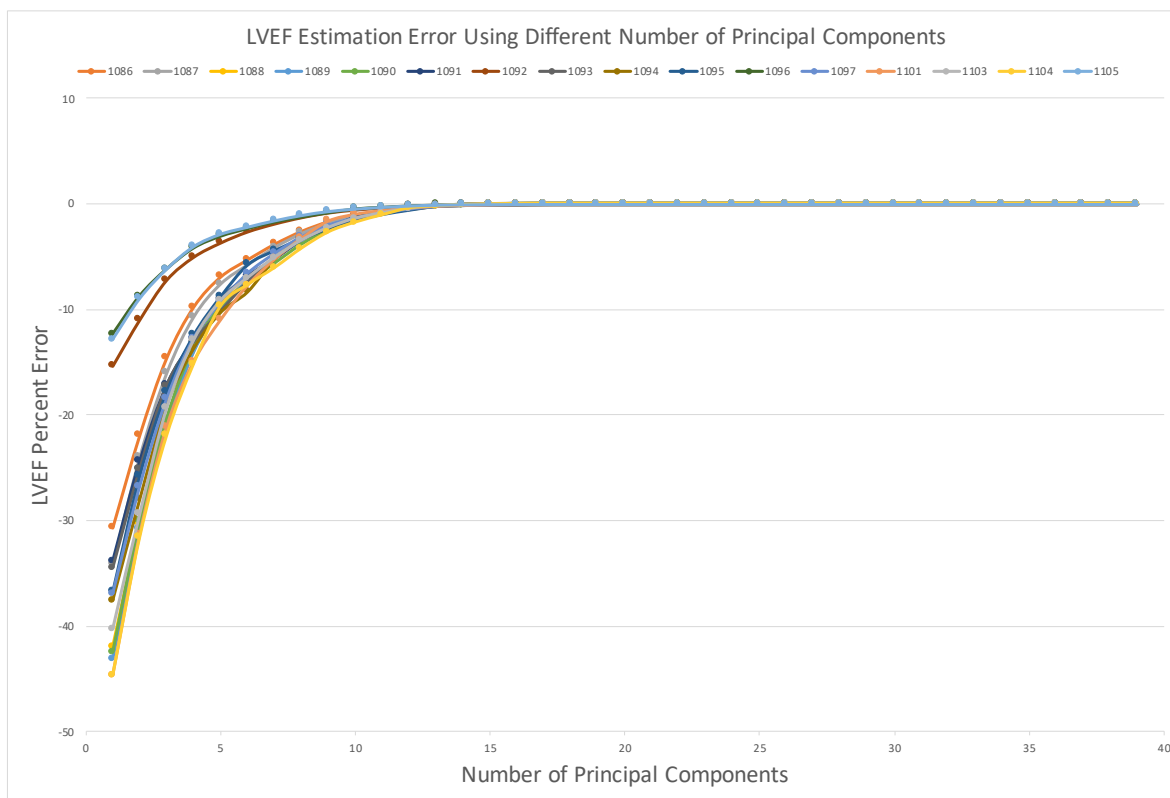


Figure 4.13: The percent difference between the LVEF computed based on SSM-estimated volumes and the LVEF computed based on the 3D reconstructed volumes using different numbers of PCs. The legend details the color codes of the data series for each of the 16 testing patient IDs.

Chapter 5

Discussion, Future Work, and Conclusion

5.1 Discussion

As Figure 4.13 illustrates, the percent errors between SSM-based LVEF calculations and the reference LVEF values are negative for all test patient image datasets. Evidently, LVEFs computed based on SSM-estimated volumes using the n -most dominant PCs consistently underestimate their corresponding reference LVEFs. However, by using at least ten most dominant PCs, a percent error less than 5% can be achieved, which is much lower than the error associated with the current visual estimates of LVEFs based on LV blood pool area changes in clinical settings.

Due to LV geometric assumptions and dimensional constraint, estimating LVEF from 2D echocardiography intrinsically leads to more inaccuracies when compared to 3D imaging modalities such as 3D echocardiography and MRI [44, 45]. Other factors that contribute to the inaccuracies include the presence of cardiac disease and subpar image quality. Ventricular dyssynchrony is a cardiac condition where the LV functions with abnormal timing and it leads to challenges in gating the image capture exactly at end-systole and end-diastole. Patients with LV dyssynchrony are associated with reduced LVEF [46] so reduced accuracy in LV

imaging accompanies the risk in failure to detect the presence of this disease. Atrial fibrillation (AF) causes irregular heart rhythm [47] and indirectly affects LVEF between heart beats. AF is problematic when multiple images of the LV are necessary to perform 3D reconstruction. In the event of AF presence, multiple measurements should be carried out so that the results could be averaged.

Image quality is often the bottleneck for a successful LV blood pool segmentation even for an experienced clinician. If the US transducer is not oriented perfectly per definitions of apical 2-chamber view, apical 3-chamber view, apical 4-chamber view, or parasternal long axis view, several artifacts could lead to inaccurate depictions of the LV blood pool. The artifacts then propagate to and affect the LV volume and LVEF calculations since they are based on multi-plane images. Our collaborator, Dr. Schwarz, suggested four attributes that contribute to the image quality of the 2D echocardiography:

1. The length, L , along the ventricular longitudinal axis connecting the apex to the mitral annulus should generally stay constant in all views at either end-systole or end-diastole.
2. The diameter at either end-systole or end-diastole, D , of the LV at mid-height along the longitudinal axis may have slight variations between tomographic views since LV is not axis-symmetric but should not vary drastically.
3. The movement, m , between LV apex at end-systole and end-diastole indicates whether the images were captured through the true apex. The closer to zero the m , the more confidence in capturing through the true apex.
4. The position, h , of the LV apex with respect to the origin in each US scan should remain at the same location to confirm that the images were captured through the true apex. These four image quality metrics can help standardize the image capture among clinicians and level the ground between experienced and inexperienced.

Furthermore, the combination of these metrics can help clinicians identify potential existence of cardiac disease instead of second-guessing whether it's an image capture problem. For

instance, if h remains constant across all views but m is significantly higher than zero, there is a high probability of LV longitudinal shortening rather than image capture misalignment.

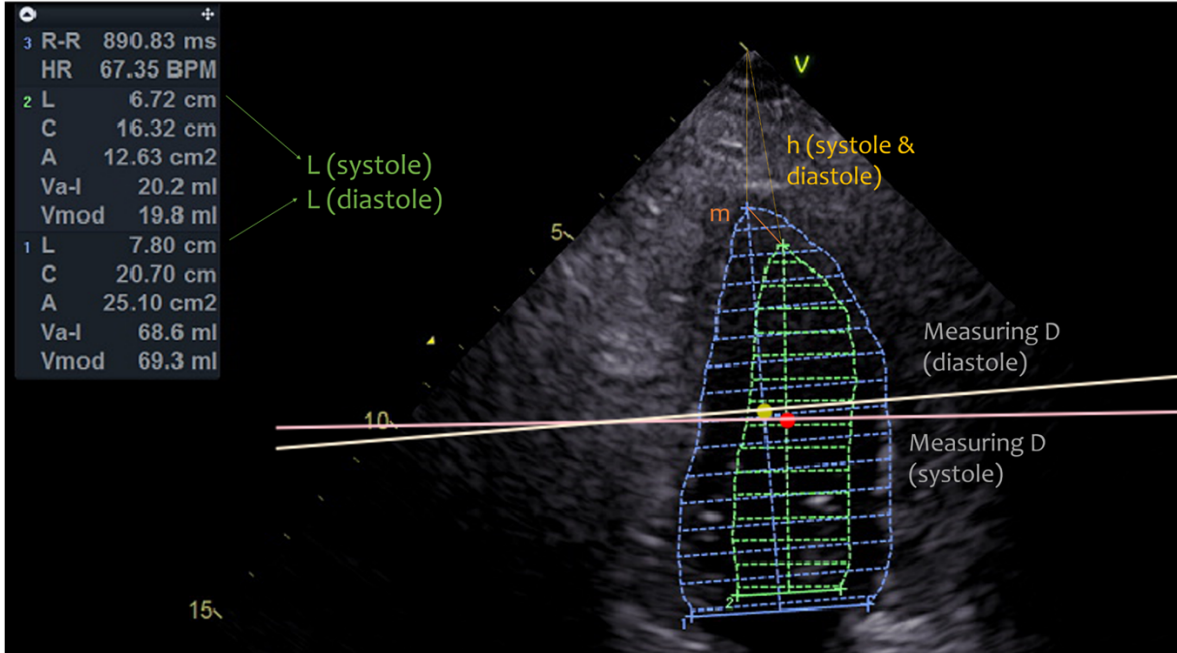


Figure 5.1: An example US image annotated with image quality metrics: L, D, m, h .

5.2 Future Work

Even though our proposed LV volume estimation method using SSM delivered promising results when compared to the reference MOD data, its accuracy of 5% error needs to be further examined for a few critical ranges of estimated values. For instance, systolic and diastolic volumes estimated from the SSM approach produce an LVEF of 63%, which is indifferent if an LVEF of 58% were reported instead for a male patient. Per Table 1.1, either reported LVEF would be considered normal. However, if an LVEF of 28% were reported instead of 33%, that is the difference between a "severely abnormal" and "moderately abnormal". Consequently, the former may lead to ventricular assist device implantation and the latter may not involve a surgical intervention at all. Such dramatically different consequence in where the inaccuracies fall in the range of LVEFs calculated from estimated LV volumes lends itself the need to conduct

a sensitivity analysis [48] as typically done on clinical trial data. Sensitivity analysis can help predict how certain variations such as outliers impact the proposed method. The challenge in determining the effect of inaccuracy of the proposed method is that appropriate ranges for the categorization of the LVEF change based on several factors of the specific patient. Thus, the threshold for a "normal" LVEF can be lower for one person than that for a "mildly abnormal" LVEF for another person. Sensitivity analysis should be conducted in coordination with more relevant definitions of LVEF categorization threshold for a specific subject.

Extending this study to a larger patient population and building a statistical shape model of the LV based on the extended patient population will enable us to study the effect of the orientation of the cross-sectional areas on the area-based LVEF estimates. Moreover, image data obtained by different clinicians should be incorporated so that intra- and inter-observer variability associated with the tracing of the LV endocardial border in both systole and diastole can be studied.

Obtaining true 3D US imaging data from our collaborating clinicians is another future effort such that the performance of our model can be further evaluated and improved. Ideally, 3D echocardiography with contrast agent image data will be obtained because of its superior image quality when compared to 2D echocardiography and non-contrast 3D echocardiography [49]. The challenge with 3D echocardiography is that the image capture spans across multiple cardiac cycles, which requires the clinician to balance between spatial and temporal resolution. Since 3D echocardiography is not as ubiquitous and often used, intra-operator variance is significant due to different levels of training [50].

Fractional shortening of the heart is common as a person ages, and it consists of long-axis and short-axis shortening [51]. When fractional shortening is present, a person's LVEF may be above the normal threshold but the absolute volume of blood pumped may be reduced. Other other hand, an athlete with enlarged ventricular size may have a lower LVEF than normal even if his or her cardiovascular performance is actually superior to an ordinary person [52]. To more comprehensively quantify a person's cardiovascular health, LV volume and LVEF should be analyzed concurrently.

Recent prevalence of machine learning (ML) techniques presents a worthwhile opportunity for a comparison to analytical approaches. Several aspects of the LVEF calculations can be automated by ML techniques such as LV blood pool segmentation [53, 54], LV geometry estimation from segmentation images, and LVEF estimation from LV geometry. Potentially, a sound ML model to estimate LVEF directly from image data is feasible eventually [55]. Such study is a Master’s project by itself but a valuable study in the age of computer-aided solutions in medical imaging.

There is also a potential application of the proposed method to be used for continuously model the LV in real-time to assist clinicians better identify the LV diastolic and systolic volumes. A possible implementation combines the knowledge and techniques from 3D deformation tracking model [56] and causality in deep learning [57]. The clinician first needs to select LV landmarks on the endocardial border as displayed on the clinical US machine, and then the SSM method can be used to estimate the appropriate 3D LV geometry. The estimated 3D LV geometry will serve as the initial model for the 3D deformation tracking, subsequent frames of the US image feed can simply use the deformation tracking model to predict the LV shape changes throughout the cardiac cycles. This approach would eliminate the need for the clinician to constantly update landmark locations by hand and the SSM-based LV shape estimations. The challenge of timing the US image capture exactly at end-systole and end-diastole can be solved by this suggested approach because systolic and diastolic LV volumes are naturally when the LV is the smallest and the biggest in the continuous LV modeling. We can also borrow the knowledge of causality in deep learning to infer what would happen to the LV geometry during the continuous modeling if certain events or variations occur.

5.3 Summary and Conclusion

Our attempt to demonstrate the necessity of quantitatively assessing LVEF rather than qualitatively estimate based on visual cues hopefully conveys the message that no shortcuts should be taken to calculating the LVEF. Using both idealized mathematical models of the LV and patient specific ultrasound imaging data, we proved that area-based LVEF estimates underes-

timate true volume-based LVEF estimates. Thus, relying on area changes as a surrogate for volume changes should not be practiced. Moreover, we also showed a method that utilizes the relative position and orientation of the multi-plane 2D US images to correctly reconstruct a more faithful representation of the LV blood pool than simply averaging three axisymmetric LV shapes. Using the reconstructed LV volumes, an SSM was constructed to establish the basis for an atlas-based LV geometry estimation method. The proposed SSM approach for estimating LV volumes and their derived LVEFs based on Mahalanobis distance and vector distance in PC space offers a viable method to efficiently obtaining accurate volume-based LVEFs. The estimated volumes help produce LVEFs estimates that are more accurate than area-based visual estimates currently used in practice. Moreover, the estimation method based on PC vector distance achieved results closer to the reference LV volume and LVEF values than the Mahalanobis distance method. The SSM-based estimation approach using PC vector distance also allows the usage of reduced number of modes of variation, and yet maintains an acceptable accuracy in the LVEF estimation. The first three and five PCs describe 71.4% and 86.5%, respectively, of the overall variances in our SSM.

In the past year, the world was turned upside down by the devastating pandemic of coronavirus disease 2019 (COVID-19). In addition to the highly infectious nature of the virus, people with cardiovascular disease are more vulnerable to the infection and likely sustain more severe symptoms. Recent research found that people with reduced LVEF are more susceptible to the SARS-CoV-2 virus [58, 59]. hence, it is more important now than ever to establish a standardized means that will help clinicians provide consistent diagnosis of cardiovascular health. The proposed solution can replace the current clinical practice that roots from non-standardized training on visually estimating LVEF from 2D US images with quantitative measurements.

Bibliography

- [1] Ultrasound. <https://www.nibib.nih.gov/science-education/science-topics/ultrasound>. (document), 1.4.3, 1.3
- [2] Russell D. Rosenberg and Pravin V. Patil. Multimodality imaging of the left ventricle: Choosing soundly. *Journal of Nuclear Cardiology*, 26(6):1865–1868, 2018. (document), 1.4
- [3] Jagdish C. Mohan and Bijoy Khandheria. *A practical approach to clinical echocardiography*. Jaypee Brothers Medical Publishers, 2014. (document), 2.1
- [4] José Sérgio Domingues, Marcos de Paula Vale, and Carlos Barreira Martinez. New mathematical model for the surface area of the left ventricle by the truncated prolate spheroid. *TheScientificWorldJournal*, 2017:6981515, 2017. (document), 2.3, 3.2
- [5] Tineke Van De Weijer, Petronella A. Van Ewijk, H. Reinier Zandbergen, Jos M. Slenter, Alfons G. Kessels, Joachim E. Wildberger, Matthijs K. C. Hesselink, Patrick Schrauwen, Vera B. Schrauwen-Hinderling, Marianne Eline Kooi, and et al. Geometrical models for cardiac mri in rodents: comparison of quantification of left ventricular volumes and function by various geometrical models with a full-volume mri data set in rodents. *American Journal of Physiology-Heart and Circulatory Physiology*, 302(3), 2012. (document), 2.2, 2.4
- [6] Karl Q. Schwarz. personal communication, 2017. 1
- [7] How does the blood circulatory system work?, Jan 2019. 1.1

- [8] Shinelle Whiteman, Yusuf Alimi, Mark Carrasco, Jerzy Gielecki, Anna Zurada, and Mar-
ios Loukas. Anatomy of the cardiac chambers: A review of the left ventricle. *Translational
Research in Anatomy*, 23:100095, 2021. 1.2
- [9] Hidekatsu Fukuta and William C Little. The cardiac cycle and the physiologic basis of
left ventricular contraction, ejection, relaxation, and filling, Jan 2008. 1.2
- [10] Ateet Kosaraju. Left ventricular ejection fraction, May 2020. 1.2
- [11] Lang RM;Badano LP;Mor-Avi V;Afilalo J;Armstrong A;Ernande L;Flachskampf
FA;Foster E;Goldstein SA;Kuznetsova T;Lancellotti P;Muraru D;Picard MH;Rietzschel
ER;Rudski L;Spencer KT;Tsang W;Voigt JU;. Recommendations for cardiac chamber
quantification by echocardiography in adults: an update from the american society of
echocardiography and the european association of cardiovascular imaging, Jan 2015. 1.3
- [12] Juan Carlos Plana, Maurizio Galderisi, Ana Barac, Michael S. Ewer, Bonnie Ky, Marielle
Scherrer-Crosbie, Javier Ganame, Igal A. Sebag, Deborah A. Agler, Luigi P. Badano, Jose
Banchs, Daniela Cardinale, Joseph Carver, Manuel Cerqueira, Jeanne M. DeCara, Thor
Edvardsen, Scott D. Flamm, Thomas Force, Brian P. Griffin, Guy Jerusalem, Jennifer E.
Liu, Andreia Magalhães, Thomas Marwick, Liza Y. Sanchez, Rosa Sicari, Hector R. Vil-
larraga, and Patrizio Lancellotti. Expert consensus for multimodality imaging evaluation
of adult patients during and after cancer therapy: a report from the American Society
of Echocardiography and the European Association of Cardiovascular Imaging. *European
Heart Journal - Cardiovascular Imaging*, 15(10):1063–1093, 10 2014. 1.3
- [13] Computed tomography (ct). [https://www.nibib.nih.gov/science-education/
science-topics/computed-tomography-ct](https://www.nibib.nih.gov/science-education/science-topics/computed-tomography-ct). 1.4.1
- [14] Magnetic resonance imaging (mri). [https://www.nibib.nih.gov/science-education/
science-topics/magnetic-resonance-imaging-mri](https://www.nibib.nih.gov/science-education/science-topics/magnetic-resonance-imaging-mri). 1.4.2

- [15] Rekha Mankad. Ejection fraction: What does it measure? Mayo Clinic, 11 February 2016 <https://www.mayoclinic.org/ejection-fraction/expert-answers/faq-20058286>. (Accessed: 21 August 2018). 1.5
- [16] Peter W. Groeneveld, Mary Anne Matta, Janice J. Suh, Paul A. Heidenreich, and Judy A. Shea. Costs and quality-of-life effects of implantable cardioverter-defibrillators. *The American Journal of Cardiology*, 98(10):1409 – 1415, 2006. 1.5
- [17] Eanna E. Flanagan and Tanja Hinderer. Constraining neutron star tidal Love numbers with gravitational wave detectors. *Phys. Rev.*, D77:021502, 2008. 1.6
- [18] Thomas A Foley, Sunil V Mankad, Nandan S Anavekar, Crystal R Bonnichsen, Michael F Miller, Todd D Morris, and Philip A Araoz. Measuring left ventricular ejection fraction – techniques and potential pitfalls. *European Cardiology Review*, 8(2):108, 2012. 2.1
- [19] Michael H. Picard, Richard L. Popp, and Arthur E. Weyman. Assessment of left ventricular function by echocardiography: A technique in evolution. *Journal of the American Society of Echocardiography*, 21(1):14–21, 2008. 2.1
- [20] M A Quinones, A D Waggoner, L A Reduto, J G Nelson, J B Young, W L Winters, L G Ribeiro, and R R Miller. A new, simplified and accurate method for determining ejection fraction with two-dimensional echocardiography. *Circulation*, 64(4):744–753, 1981. 2.1
- [21] Louis Evan Teichholz, Thomas Kreulen, Michael V. Herman, and Richard Gorlin. Problems in echocardiographic volume determinations: Echocardiographic-angiographic correlations in the presence or absence of asynergy. *The American Journal of Cardiology*, 37(1):7–11, 1976. 2.1
- [22] Suresh Chengode. Left ventricular global systolic function assessment by echocardiography. *Annals of Cardiac Anaesthesia*, 19(5):26, 2016. 2.1
- [23] Sushil A. Luis, Jonathan Chan, and Patricia A. Pellikka. Echocardiographic assessment of left ventricular systolic function: An overview of contemporary techniques, including speckle-tracking echocardiography. *Mayo Clinic Proceedings*, 94(1):125–138, 2019. 2.1

- [24] JG Dumesnil, RM Shoucri, JL Laurenceau, and J Turcot. A mathematical model of the dynamic geometry of the intact left ventricle and its application to clinical data. *Circulation*, 59(5):1024–1034, May 1979. 2.2, 3.2
- [25] Paulo Roberto Pinto Ferreira Filho. Padrões de hipertrofia e geometria do ventrículo esquerdo pela ecocardiografia transtorácica. *Revista Brasileira de ecocardiografia e Imagem Cardiovascular*, 25(2):103–115, 2012. 2.2
- [26] Liang Zhong, Yi Su, Si-Yong Yeo, Ru-San Tan, Dhanjoo N. Ghista, and Ghassan Kassab. Left ventricular regional wall curvedness and wall stress in patients with ischemic dilated cardiomyopathy. *American Journal of Physiology-Heart and Circulatory Physiology*, 296(3):H573–H584, 2009. PMID: 19122166. 2.2, 3.2
- [27] H Sawada, J Fujii, K Kato, M Onoe, and Y Kuno. Three dimensional reconstruction of the left ventricle from multiple cross sectional echocardiograms. value for measuring left ventricular volume. *Heart*, 50(5):438–442, 1983. 2.3
- [28] Honggang Yu, Marios S. Pattichis, and M. Beth Goens. Multi-view 3d reconstruction with volumetric registration in a freehand ultrasound imaging system. *Medical Imaging 2006: Ultrasonic Imaging and Signal Processing*, 2006. 2.3
- [29] Chenyang Xu and J.I. Prince. Gradient vector flow: a new external force for snakes. *Proceedings of IEEE Computer Society Conference on Computer Vision and Pattern Recognition*. 2.3
- [30] C Bonciu, R Weber, and C Léger. 4d reconstruction of the left ventricle during a single heart beat from ultrasound imaging. *Image and Vision Computing*, 19(6):401–412, 2001. 2.3
- [31] Robert J. Ii. Marks. *Introduction to shannon sampling and interpolation theory*. Springer, 2012. 2.3
- [32] Judy Hung, Roberto Lang, Frank Flachskampf, Stanton K. Shernan, Marti L. McCulloch, David B. Adams, James Thomas, Mani Vannan, and Thomas Ryan. 3d echocardiography:

- A review of the current status and future directions. *Journal of the American Society of Echocardiography*, 20(3):213–233, 2007. 2.3
- [33] G. Coppini, R. Poli, and G. Valli. Recovery of the 3-d shape of the left ventricle from echocardiographic images. *IEEE Transactions on Medical Imaging*, 14(2):301–317, 1995. 2.3
- [34] Jan L. Bruse, Hopewell Ntsinjana, Claudio Capelli, Giovanni Biglino, Kristin McLeod, Maxime Sermesant, Xavier Pennec, Tain-Yen Hsia, Silvia Schievano, and Andrew Taylor. Cmr-based 3d statistical shape modelling reveals left ventricular morphological differences between healthy controls and arterial switch operation survivors. *Journal of Cardiovascular Magnetic Resonance*, 18, 2016. 2.4
- [35] Genevieve Farrar, Avan Suinesiaputra, Kathleen Gilbert, James C. Perry, Sanjeet Hegde, Alison Marsden, Alistair A. Young, Jeffrey H. Omens, and Andrew D. McCulloch. Atlas-based ventricular shape analysis for understanding congenital heart disease. *Progress in Pediatric Cardiology*, 43:61 – 9, 2016. 2.4
- [36] Pau Medrano-Gracia, Brett R. Cowan, Bharath Ambale-Venkatesh, David A. Bluemke, John Eng, John Paul Finn, Carissa G. Fonseca, Joao AC Lima, Avan Suinesiaputra, and Alistair A. Young. Left ventricular shape variation in asymptomatic populations: the multi-ethnic study of atherosclerosis. *Journal of Cardiovascular Magnetic Resonance*, 16:56, 2014. 2.4
- [37] Pau Medrano-Gracia, Brett R. Cowan, J. Paul Finn, Carissa G. Fonseca, Alan H. Kadish, Dan C. Lee, Wenchao Tao, and Alistair A. Young. The cardiac atlas project: Preliminary description of heart shape in patients with myocardial infarction. In Oscar Camara, Mihaela Pop, Kawal Rhode, Maxime Sermesant, Nic Smith, and Alistair Young, editors, *Statistical Atlases and Computational Models of the Heart*, pages 46–53, 2010. 2.4

- [38] E. W. Remme, A. A. Young, K. F. Augenstein, B. Cowan, and P. J. Hunter. Extraction and quantification of left ventricular deformation modes. *IEEE Transactions on Biomedical Engineering*, 51:1923–31, 2004. 2.4
- [39] Shai Tejman-Yarden, Andras Bratincsak, Noa Bachner-Hinenzon, Hanan Khamis, Callie Rzasa, Dan Adam, Beth F. Printz, and James C. Perry. Left ventricular mechanical property changes during acute av synchronous right ventricular pacing in children. *Pediatric Cardiology*, 37:106–111, 2016. 2.4
- [40] Xingyu Zhang, Brett R. Cowan, David A. Bluemke, J. Paul Finn, Carissa G. Fonseca, Alan H. Kadish, Daniel C. Lee, Joao A. C. Lima, Avan Suinesiaputra, Alistair A. Young, and Pau Medrano-Gracia. Atlas-based quantification of cardiac remodeling due to myocardial infarction. *PLOS ONE*, pages 1–13, 2014. 2.4
- [41] Kenneth Horton. Basic ultrasound views. 01 2010. 3.1
- [42] S. Dangi, Y. K. Ben-Zikri, N. Cahill, K. Q. Schwarz, and C. A. Linte. Endocardial left ventricle feature tracking and reconstruction from tri-plane trans-esophageal echocardiography data. In *Medical Imaging 2015: Image-Guided Procedures, Robotic Interventions, and Modeling*, volume 9415, page 941505, March 2015. 3.3
- [43] G. Mclachlan. Mahalanobis distance. *Resonance*, 4:20–26, 06 1999. 3.4.1
- [44] Carly Jenkins, Kristen Bricknell, Jonathan Chan, Lizelle Hanekom, and Thomas H. Marwick. Comparison of two- and three-dimensional echocardiography with sequential magnetic resonance imaging for evaluating left ventricular volume and ejection fraction over time in patients with healed myocardial infarction. *The American Journal of Cardiology*, 99(3):300–306, 2007. 5.1
- [45] Ebere O. Chukwu, Eddy Barasch, Dennis G. Mihalatos, Alan Katz, Justine Lachmann, Jing Han, Nathaniel Reichel, and Aasha S. Gopal. Relative importance of errors in left ventricular quantitation by two-dimensional echocardiography: Insights from three-

- dimensional echocardiography and cardiac magnetic resonance imaging. *Journal of the American Society of Echocardiography*, 21(9):990–997, 2008. 5.1
- [46] A. B. S. Santos, E. Kraigher-Krainer, N. Bello, B. Claggett, M. R. Zile, B. Pieske, A. A. Voors, J. J. V. McMurray, M. Packer, T. Bransford, and et al. Left ventricular dyssynchrony in patients with heart failure and preserved ejection fraction. *European Heart Journal*, 35(1):42–47, 2013. 5.1
- [47] Atrial fibrillation, Sep 2020. 5.1
- [48] Lehana Thabane, Lawrence Mbuagbaw, Shiyuan Zhang, Zainab Samaan, Maura Marcucci, Chenglin Ye, Marroon Thabane, Lora Giangregorio, Brittany Dennis, Daisy Kosa, and et al. A tutorial on sensitivity analyses in clinical trials: the what, why, when and how. *BMC Medical Research Methodology*, 13(1), 2013. 5.2
- [49] Peter W. Wood, Jonathan B. Choy, Navin C. Nanda, and Harald Becher. Left ventricular ejection fraction and volumes: It depends on the imaging method. *Echocardiography*, 31(1):87–100, 2013. 5.2
- [50] V. Mor-Avi, C. Jenkins, H. Kuhl, H.j. Nesser, T.h. Marwick, A. Franke, C. Ebner, B.h. Freed, R. Steringer-Mascherbauer, H. Pollard, and et al. Real-time 3d echocardiographic quantification of left ventricular volumes: Multicenter study for validation with magnetic resonance imaging. *2008 Computers in Cardiology*, 2008. 5.2
- [51] Asbjørn Støylen, Håvard Dalen, and Harald Edvard Molmen. Left ventricular longitudinal shortening: relation to stroke volume and ejection fraction in ageing, blood pressure, body size and gender in the hunt3 study. *Open Heart*, 7(2), 2020. 5.2
- [52] Admin. 3.2.3 left ventricular function. *123 Sonography*, Jan 2019. 5.2
- [53] Erik Smistad, Andreas Ostvik, Bjorn Olav Haugen, and Lasse Lovstakken. 2d left ventricle segmentation using deep learning. *2017 IEEE International Ultrasonics Symposium (IUS)*, 2017. 5.2

- [54] G. Carneiro and J. C. Nascimento. Combining multiple dynamic models and deep learning architectures for tracking the left ventricle endocardium in ultrasound data. *IEEE Transactions on Pattern Analysis and Machine Intelligence*, 35(11):2592–2607, 2013. 5.2
- [55] Federico M. Asch, Nicolas Poilvert, Theodore Abraham, Madeline Jankowski, Jayne Cleve, Michael Adams, Nathanael Romano, Ha Hong, Victor Mor-Avi, Randolph P. Martin, and et al. Automated echocardiographic quantification of left ventricular ejection fraction without volume measurements using a machine learning algorithm mimicking a human expert. *Circulation: Cardiovascular Imaging*, 12(9), 2019. 5.2
- [56] Hanbyul Joo, Tomas Simon, and Yaser Sheikh. Total capture: A 3d deformation model for tracking faces, hands, and bodies. *2018 IEEE/CVF Conference on Computer Vision and Pattern Recognition*, 2018. 5.2
- [57] Bernhard Schölkopf, Francesco Locatello, Stefan Bauer, Nan Rosemary Ke, Nal Kalchbrenner, Anirudh Goyal, and Yoshua Bengio. Towards causal representation learning, 2021. 5.2
- [58] Kensuke Matsushita, Benjamin Marchandot, Adrien Carmona, Anais Curtiaud, Anis El Idrissi, Antonin Trimaille, Marion Kibler, Thomas Cardi, Joe Heger, Sebastien Hess, and et al. Increased susceptibility to sars-cov-2 infection in patients with reduced left ventricular ejection fraction. *ESC Heart Failure*, 8(1):380–389, 2020. 5.3
- [59] Laurie Soulat-Dufour, Sylvie Lang, Stephane Ederhy, Saroumadi Adavane-Scheuble, Marion Chauvet-Droit, Pascal Nhan, Marie-Liesse Jean, Rim Ben Said, Pauline Issaurat, Franck Boccara, and et al. Left ventricular ejection fraction: An additional risk marker in covid-19. *Archives of Cardiovascular Diseases*, 113(11):760–762, 2020. 5.3